INTERSTELLAR DUST MODELS CONSISTENT WITH EXTINCTION, EMISSION, AND ABUNDANCE CONSTRAINTS

Viktor Zubko[1,2], Eli Dwek, and Richard G. Arendt[2]

NASA Goddard Space Flight Center, Code 685, Greenbelt, MD 20771

ABSTRACT

We present new interstellar dust models which have been derived by simultaneously fitting the far–ultraviolet to near–infrared extinction, the diffuse infrared (IR) emission and, unlike previous models, the elemental abundance constraints on the dust for different interstellar medium abundances, including solar, F and G star, and B star abundances. The fitting problem is a typical ill-posed inversion problem, in which the grain size distribution is the unknown, which we solve by using the method of regularization. The dust model contains various components: PAHs, bare silicate, graphite, and amorphous carbon particles, as well as composite particles containing silicate, organic refractory material, water ice, and voids. The optical properties of these components were calculated using physical optical constants. As a special case, we reproduce the Li & Draine (2001) results, however their model requires an excessive amount of silicon, magnesium, and iron to be locked up in dust: about 50 ppm (atoms per million of H atoms), significantly more than the upper limit imposed by solar abundances of these elements, about 34, 35, and 28 ppm, respectively. A major conclusion of this paper is that there is no unique interstellar dust model that simultaneously fits the observed extinction, diffuse IR emission, and abundances constraints. We find several classes of acceptable interstellar dust models, that comply with these constraints. The first class is identical in composition to the Li & Draine model, consisting of PAHs, bare graphite and silicate grains, but with a different size distribution that is optimized to comply with the abundances constraints. The second class of models contains in addition to PAHs bare graphite and silicate grains also composite particles. Other classes contain amorphous carbon instead of graphite particles, or no carbon at all, except for that in PAHs. All

---

[1]Corresponding author: `zubko@stars.gsfc.nasa.gov`

[2]Science Systems and Applications, Inc.

classes are consistent with solar and F & G star abundances, but have greater difficulty fitting the B star carbon abundance, which is better fit with the latter (no carbon) models. Additional observational constraints, such as the interstellar polarization, or x–ray scattering may be able to discriminate between the various interstellar dust models.

Subject headings: dust, extinction — infrared: ISM — ISM: abundances — ultraviolet: ISM

1.   INTRODUCTION

Interstellar dust is completely characterized by the composition, morphology, and size distribution of its various particles, and by the abundance, relative to hydrogen, of its elemental constituents. A viable dust model should be able to explain the various astrophysical phenomena associated with the presence of dust in the interstellar medium (ISM): the wavelength dependence of the interstellar extinction, albedo, and polarization, the infrared emission, and the observed elemental depletion pattern as primary constraints, and the extended red emission (ERE) as a secondary constraint. Dust characteristics may vary in the different ISM phases and Galactic locations. Here we concentrate on characterizing the dust in the local diffuse ISM.

Interstellar dust models have evolved with the advance of observational data. Until recently, the most popular dust model was the Mathis, Rumple, & Nordsieck (1977; hereafter MRN), which, using the dust optical constants of Draine & Lee (1984) provided an excellent fit to the average interstellar extinction curve. The model consisted of a population of spherical graphite and silicate dust particles with a $a^{-3.5}$ power–law distribution in grain radii in the $\{a_{\mathrm{min}}, a_{\mathrm{max}}\} = \{0.005~\mu\mathrm{m}, 0.25~\mu\mathrm{m}\}$ size interval. Assuming solar composition for the ISM, the model required essentially all the interstellar carbon, C/H = 370 ppm (parts per million), and all the magnesium, silicon, and iron, Mg/H, Si/H, Fe/H = $\{34, 35, 28\}$, to be locked up in dust.

The first observational evidence for the incompleteness of the MRN dust model was provided by the *Infrared Astronomical Satellite* (*IRAS*) all sky survey, which provided the average infrared (IR) emission spectrum at 12, 25, 60, and 100 μm from the diffuse ISM. The observations showed an excess of 12 and 25 μm emission over that expected from dust heated by the local interstellar radiation field (ISRF) and radiating at the equilibrium dust temperature. Draine & Anderson (1985) suggested that the MRN grain size distribution should be extended to very small grains (VSG) with radii of ~ 5 Å which undergo temper-

ature fluctuations when heated by the ISRF. Allamandola, Tielens, & Barker (1985), and Léger & Puget (1984) identified these VSG with polycyclic aromatic hydrocarbon (PAH) molecules whose presence in the ISM was inferred from the ubiquitous solid state emission features at 3.3, 6.7, 7.6, 8.6, and 11.3 μm. We point out that the identification of PAHs with these IR features is not universally accepted [see Tokunaga (1997) for a review].

The *IRAS* observations pointed out the importance of the IR emission as a constraint on interstellar dust models. The first model that attempted to fit in a self-consistent manner the interstellar extinction as well as the diffuse IR emission using PAHs as an interstellar dust component was the model of Désert, Boulanger, & Puget (1990). However, their model did not use physical optical constants for the various dust components, and was primarily empirical in nature.

Interstellar polarization provides addtional constraints on interstellar dust particles (Kim & Martin 1995, 1996; Li & Greenberg 1997). In particular, the latter authors presented a interstellar dust model consisting of PAHs, and cylindrical silicates coated with an organic refractory mantle. Their model satisfies the interstellar extinction, polarization and solar abundances constraints. It did not attempt to fit the diffuse IR emission, and used particles with hypothetical optical constants to represent the far-UV extinction and the 2200 Å extinction hump.

The Diffuse IR Background Experiment (DIRBE) and Far Infrared Absolute Spectrophotometer (FIRAS) instrument on board the *Cosmic Background Explorer* (*COBE*) satellite provided the most extensive wavelength coverage (3.5 to 1000 μm) of the IR emission from the diffuse ISM, and indirect evidence for the emission from PAHs from this phase of the medium (Dwek et al. 1997). Dwek et al. (1997) attempted to fit the interstellar extinction and diffuse IR emission using a mix of bare silicate and graphite particles with Draine & Lee (1984) optical constants, and PAHs with the optical properties of Désert et al. (1990). The model failed to reproduce the observed interstellar extinction, primarily due to the non-physical nature of the UV-optical properties adopted for the PAHs. Draine & Li (2001) and Li & Draine (2001b) improved on this model by using a more realistic characterization of the optical properties of the PAHs, based on laboratory measurements. However, their model requires an excessive amount of Mg, Si, and Fe to be locked up in dust, almost twice the available iron for an ISM with solar abundances.

In this paper we explore possible dust models that simultaneously comply with the three major observational constraints: the average interstellar extinction, the thermal IR emission form the diffuse ISM, and the interstellar abundances constraints. The model explores a variety of potential dust compositions, including bare silicate ($MgFeSiO_4$), graphite, amorphous carbon particles, PAHs, and composite particles consisting of a mixture of silicate, refractory

organic material (C:H:O:N $\approx$ 1:1:0.2:0.04; we will adopt $C_{25}H_{25}O_5N$ for simplicity), water ice (H_2O), and voids. The model is physical in the sense that it uses measured optical constants or observed radiative properties to characterize the optical properties of the various dust constituents. Given the composition and physical properties of the dust particles, the problem of simultaneously fitting the model to a set of observational constraints is a typical ill-posed inversion problem, in which the grain size distribution is the unknown. We solve this problem using the method of regularization.

In §2 we present the integral equation that we invert in order to solve for the grain size distribution. The general equations for the interstellar extinction, IR emission, and elemental dust abundances are cast as a Fredholm integral equation of the first kind. The left hand side (LHS) in the equation comprises of the observational input data, and the RHS is an integral over grain sizes of a known function, the kernel, multiplied by an unknown fuction, the grain size distribution. The section summarizes the observational input data used in our analysis: the average interstellar extinction, thermal IR emission per H atom, the average interstellar radiation field (ISRF) to which the dust is exposed, and the allowable amount of refractory elements that can be locked up in the dust, and the physical properties of the dust that are used in the kernel. §3 describes the Regularization method that we used to invert the Fredholm equation to derive the distribution of grain sizes that satisfies the observational constraints for a given kernel. Modeling details are presented in §4. The results of our calculations are presented in §5. We show that the Li & Draine PAH, bare silicate, and graphite model can be optimized, and we produce an equally good fit to the observational constraints without violating the interstellar abundance constraints for a different, more general, grain size distribution. We also show that the PAH, bare silicate and graphite grain model is not unique. A more complex dust model comprising of PAHs, bare silicate and graphite grains, as well as organic refractory and icy silicates, provides a somewhat improved fit to the observational constraints, including the interstellar abundances. A summary of the paper, its astrophysical implications, and directions for future improvements and tests for interstellar dust models are presented in §§6 and 7.

2. THEORETICAL MODEL

2.1. Constructing the Main Integral Equation

The goal of our studies is to find dust models that simultaneously fit the observed interstellar extinction, infrared emission, and elemental abundance constraints. A dust model consists of a set of dust components ($i = 1..n$) each of which is characterized by a chemical composition and a size distribution function $f_i(a)\,\mathrm{d}a$, defined as the number of grains per

hydrogen (H) atom in the radius interval a to $a + \mathrm{d}a$. Thus, if ρ_i is the mass density of i-th component, the expressions $\sum_{i=1}^{n} \int f_i(a)\,\mathrm{d}a$ and $\sum_{i=1}^{n} \int \frac{4}{3}\pi a^3 \rho_i f_i(a)\,\mathrm{d}a$, give, respectively, the total number of dust particles per H atom and their total mass per H atom, summed up over all dust components.

The observational constraints we use to characterize the nature of the dust in the diffuse ISM are:

1. the average wavelength-dependent extinction $\tau(\lambda)$ per H column density:

$$\frac{\tau(\lambda)}{N_{\mathrm{H}}} = \sum_{i=1}^{n} \int \left[\pi a^2\, Q_{\mathrm{ext}}^{[i]}(\lambda, a) \right] f_i(a)\,\mathrm{d}a \equiv \sum_{i=1}^{n} \int K_{\tau}^{[i]}(\lambda, a)\, f_i(a)\,\mathrm{d}a \tag{1}$$

where N_{H} is the line-of-sight hydrogen column density, and $Q_{\mathrm{ext}}^{[i]}(\lambda, a)$ is the extinction efficiency of the i-th component of radius a.

2. the spectrum and intensity of the infrared emission from the diffuse ISM:

$$\frac{I_\lambda(\lambda)}{N_{\mathrm{H}}} = \sum_{i=1}^{n} \int \left[\pi a^2\, Q_{\mathrm{abs}}^{[i]}(\lambda, a)\, E_\lambda^{[i]}(\lambda, a) \right] f_i(a)\,\mathrm{d}a \equiv \sum_{i=1}^{n} \int K_I^{[i]}(\lambda, a)\, f_i(a)\,\mathrm{d}a \tag{2}$$

where $I_\lambda(\lambda)$ is the specific intensity per unit solid angle, $Q_{\mathrm{abs}}^{[i]}(\lambda, a)$ is the absorption efficiency factor at λ of the i-th dust component of radius a, and $E_\lambda^{[i]}(\lambda, a)$ is its emissivity. For all dust particles $E_\lambda^{[i]}(\lambda, a)$ is given by:

$$E_\lambda(\lambda, a) = \int_{\frac{hc}{\lambda}}^{\infty} \mathrm{d}U\, P(a, U)\, B_\lambda[\lambda, T(U, a)], \tag{3}$$

where $T[U, a]$ is the vibrational temperature of the dust with an internal energy U, and $P(a, U)$ is the probability distribution of internal energy U for grains of radius a. Very small dust particles will be stochastically heated by the interstellar radiation field and undergo temperature, or internal energy fluctuations which were first predicted by Greenberg (1968). For sufficiently large grains with the thermal content significantly exceeding the mean energy of the colliding photons, $P(a, U)$ can be approximated by a delta function at U_{eq} corresponding to an equilibrium temperature $T_{\mathrm{eq}}(a)$. In this case, $E_\lambda(\lambda, a)$ is simply the Planck function:

$$E_\lambda(\lambda, a) \simeq B_\lambda[\lambda, T_{\mathrm{eq}}(a)]. \tag{4}$$

The grain equilibrium temperature is defined by the balance of absorbed and emitted radiation:

$$\int_0^{\infty} \pi a^2\, Q_{\mathrm{abs}}(\lambda, a)\, J_\lambda^{\mathrm{ISRF}}(\lambda)\,\mathrm{d}\lambda = \int_0^{\infty} \pi a^2\, Q_{\mathrm{abs}}(\lambda, a)\, B_\lambda[\lambda, T_{\mathrm{eq}}(a)]\,\mathrm{d}\lambda. \tag{5}$$

where $J_\lambda^{\mathrm{ISRF}}(\lambda)$ is the intensity of the local interstellar radiation field (ISRF).

3. the abundance of elements locked up in the solid phase of the diffuse ISM. If k is the number of chemical elements constituing the dust, then the column density N_j of the j-th element ($j = 1..k$) locked up in the dust is given by:

$$\frac{N_j}{N_{\rm H}} = \sum_{i=1}^{n} \int \left[\frac{4}{3} \pi a^3 \, \rho_i \frac{\alpha_{j,i}}{m_j} \right] f_i(a) \, {\rm d}a \equiv \sum_{i=1}^{n} \int K_j^{[i]}(a) \, f_i(a) \, {\rm d}a \tag{6}$$

where m_j is the atomic mass of j-th element, and $\alpha_{j,i}$ is the mass fraction of j-th element in the i-th constituent. For example, for silicon locked up in olivine [(Mg,Fe)$_2$SiO$_4$ or else MgFeSiO$_4$ to imply that $N_{\rm Mg}=N_{\rm Fe}$ in the grain composition], $m_j = 28 \, m_{\rm H}$ and $\alpha_{j,i} = 28/172$.

K_τ, K_I, and K_j, $j=\{1..k\}$, defined in equations (1), (2), and (6), can be combined into one superkernel $K(x,a)$, given by:

$$
\begin{aligned}
K(x,a) \quad = \quad & [\{K_\tau^{[1]}(\lambda^{\rm ext},a),\ldots,K_\tau^{[n]}(\lambda^{\rm ext},a)\}, \{K_I^{[1]}(\lambda^{\rm em},a),\ldots,K_I^{[n]}(\lambda^{\rm em},a)\}, \\
& \{K_1^{[1]}(a),\ldots,K_1^{[n]}(a)\},\ldots,\{K_k^{[1]}(a),\ldots,K_k^{[n]}(a)\}],
\end{aligned}
\tag{7}
$$

where x is a generalized variable: $x = \{\lambda^{\rm ext}, \lambda^{\rm em}, j\}$, which runs the wavelengths of the extinction data: $\lambda^{\rm ext} = \lambda_{\rm min}^{\rm ext},\ldots,\lambda_{\rm max}^{\rm ext}$, then the wavelengths of the emission spectrum data: $\lambda^{\rm em} = \lambda_{\rm min}^{\rm em},\ldots,\lambda_{\rm max}^{\rm em}$, and, finally, the number of the abundance constraints: $j = 1,\ldots,k$. Since equations (1), (2), and (6) are linearly dependent on the grain size distribution $f_i(a)$, we can combine them into a single integral equation as:

$$D(x) = \int K(x,a) \, F(a) \, {\rm d}a, \tag{8}$$

where $D(x)$ consists of the observational constraints:

$$D(x) = [\tau(\lambda^{\rm ext}), I_\lambda(\lambda^{\rm em}), N_j]/N_{\rm H}, \tag{9}$$

and $F(a)$ is an array of the size distribution functions given by:

$$F(a) = [f_1(a),\ldots,f_n(a)], \tag{10}$$

In the following we describe the observational constraints and the dust model assumptions needed, respectively, to define $D(x)$ and calculate $K(x,a)$. In addition to $D(x)$ and $K(x,a)$, the inversion of equation (8) will require knowledge of the uncertainties, $\sigma(x)$, in $D(x)$, which are defined in terms of the uncertainties in the different observational constraints as:

$$\sigma(x) = [\sigma_\tau(\lambda^{\rm ext}), \sigma_I(\lambda^{\rm em}), \sigma_{N_j}] \tag{11}$$

2.2. Observational Constraints, $D(x)$ and Uncertainties, $\sigma(x)$

We used the latest available mean extinction curve for R_V=3.1 from Fitzpatrick (1999) to characterize the average extinction from the diffuse ISM. In contrast to previous extinction curves [e.g. by Cardelli et al. (1989) or Savage & Mathis (1979)], the new curve has been constructed to reproduce the detailed wavelength behavior of the extinction for R_V=3.1 by properly taking into account the bandpass effects in optical/IR data and the observed broadband, intermediate-band, and narrow-band extinction measurements. Note that a new far-UV Galactic extinction curve from 910 to 1200 Å reported by Sasseen et al. (2002) shows a good consistency with Fitzpatrick's curve. Figure 1 displays the extinction curve in the form of $\tau_{\rm ext}/N_{\rm H}$ that we used for our modeling. It was derived by us from the original $E(\lambda-V)/E(B-V)$ curve by using the ratio $N_{\rm H}/E(B-V) = 5.8\times10^{21}$ H cm^{-2} typical for the diffuse ISM (Bohlin et al. 1978). Also shown in the figure is the new far-UV extinction curve from 910 to 1200 Å reported by Sasseen et al. (2002) and the 912 Å to 3.5 μm extinction curve of Cardelli et al. (1989). We note that Li & Draine (2001b) used a different normalization of the curve at $I(0.9\ \mu$m) band, given by: $A(I)/N_{\rm H} = 2.6\times10^{-22}$ cm^2 (Draine 1989). This produces a factor of 1.12 difference between their adopted extinction curve and ours. The uncertainties on Figure 1 are the observed dispersion of the curve. The estimate in the UV-through-optical segment is based on the *ANS* satellite work by Savage et al. (1985) covering about 1000 sightlines. The uncertainty in the infrared part was estimated supposing the R_V dispersion of 0.4 to 0.5, which is consistent with the observed scatter of the extinction curve at 1500 Å (Fitzpatrick 1999).

The *COBE* all sky survey provided the most comprehensive spectrum of dust emission from the diffuse ISM in eight DIRBE bands at 3.5, 4.9, 12, 25, 60, 100, 140, and 240 μm, and in the FIRAS channels spanning the $\sim$ 200 and 1000 μm wavelength range (Dwek et al. 1997; Arendt et al. 1998). Figure 2 shows the average IR emission from the diffuse ISM used by us to constrain the dust models. The uncertainties of the DIRBE fluxes are from Dwek et al. (1997).

Since the chemical composition of the dust cannot be directly measured, it is common to estimate the abundance of an element locked up in dust by subtracting the observed gas phase abundance of that element from an adopted measure of its total ISM abundance. The latter is determined from stellar surface abundances which are believed to represent the total abundance of that element in the gas and dust phases of the ISM from which those stars have formed. Due to the uncertainties in the choice of a representative set of average ISM abundances we have used three different measurements based on solar (Holweger 2001), B star (Snow & Witt 1996; Sofia & Meyer 2001), and F and G star (Sofia & Meyer 2001) abundances to characterize the standard abundances of the elements in the ISM. Figure 3

and Table 1 summarizes the abundances of the most abundant elements expected to be in the dust: C, O, Si, Mg, Fe, and N. Also shown in the table are the measured gas phase abundances of these elements. The dust phase abundances used to constrain the dust models are simply the ISM minus the gas phase abundances for the different elements. Because of the large discrepancy between the two available estimates of the gas-phase C of 140±20 (Cardelli et al. 1996) and 75±25 (Dwek et al. 1997), we adopted a single estimate of 108±16 that is a straight average of the two values.

2.3. Dust Model and Grain Emissivities, $K(x, a)$

Several dust compositions were used to characterize the interstellar dust population: (1) *bare silicate and graphite grains* with optical constants of Draine & Lee (1984), Laor & Draine (1993), and Weingartner & Draine (2001); (2) *polycyclic aromatic hydrocarbons (PAHs)* with specific density of 2.24 g cm^{-3}, and absorption cross sections from Li & Draine (2001b); and (3) *amorphous carbon dust.* We tried three different types of amorphous carbon: ACAR, BE, and ACH2[3] with the optical constants from Zubko et al. (1996b). In addition to these dust constituents, we also considered composite particles composed of silicate, amorphous carbon, and variations of the following components: (1) *organic refractory material* consisting of [C$_{25}$H$_{25}$O$_5$N] with optical constants from Li & Greenberg (1997); (2) *water ice*, with optical constants from Warren (1984); and (3) *voids*. Table 2 summarizes the properties of the different dust constituents used in this paper.

Like Li & Draine (2001b), we treat PAHs and graphite as different dust components. However, we allow for the extension of the graphite grain size distribution to very small particles. Very small graphite particles are essentially dehydrated PAHs. In contrast, Li & Draine extend the graphite size distribution only down to 50 Å, and adopt PAH-like properties for carbonaceous particles with sizes below ∼20 Å. As we will show in §5.1, as a result of this difference we derive a carbonaceous grain size distribution that is considerably simpler than that of Li & Draine (2001b).

To build $K(x, a)$, we need to know the extinction and absorption cross sections: $Q_{\text{ext}}^{[i]}(\lambda, a)$, $Q_{\text{abs}}^{[i]}(\lambda, a)$, emissivities $E_\lambda^{[i]}(\lambda, a)$, densities ρ_i, and mass fractions α_{ji}. The densities used are listed in Table 2, the mass fractions are easily calculated by using atomic and molecular

---

[3]ACAR sample was produced in arc discharge between amorphous carbon electrodes in an Ar atmosphere at 10 mbar; ACH2 sample was produced in arc discharge between amorphous carbon electrodes in an H$_2$ atmosphere at 10 mbar; BE sample was produced by burning of benzene in air under normal consitions (Colangeli et al. 1995)

masses of dust constituents.

For the bare silicate, graphite, and amorphous carbon particles, the extinction and absorption cross sections were calculated using Mie theory for spherical dust particles (Bohren & Huffman 1983). For the composite material, at first step, we used an effective medium theory (EMT) to calculate its dielectric function, and, at second step, we used Mie theory to calculate the absorption and scattering cross sections with the effective dielectric function. The effective dielectric function was calculated by making use of an EMT based on the Bruggeman approach with adjusted effective shape factors (EMT-O), that gives the following equation for the effective dielectric function ε_{eff} (Stognienko et al. 1995):

$$\sum_k \sum_{l=1}^{4} f_l^k \frac{\varepsilon^k - \varepsilon_{\text{eff}}}{\varepsilon_{\text{eff}} + (\varepsilon^k - \varepsilon_{\text{eff}})L_l^k} = 0 \tag{12}$$

with $L_l^k = \{0, 1/2, 1, 1/3\}$, $f_1^k = (5/9)f^k \sin^2(\pi f^k)$, $f_2^k = (2/9)f^k \sin^2(\pi f^k)$, $f_3^k = (2/9)f^k \sin^2(\pi f^k)$, $f_4^k = f^k \cos^2(\pi f^k)$, where f^k and ε^k are the volume fraction and isotropic dielectric function of component k, and L_l^k are some shape factors for ellipsoidal grains. Equation (12) is an approximation to different experiments and theories. The EMT-O approach takes into consideration the effects of shape distribution, proximity, connected particles and percolation, and thus it is highly suitable for treating the composite particles which are the aggregates of clustered grains. For example, the percolated structure of the composites is simulated by "particles" with shape factor 0. It is easy to show that in the limit when cells of all components of the composites have spherical shape ($L_l^k = \frac{1}{3}$ and $f_l^k = f^k$), the EMT-O rule (eq. 12) reduces to the classical Bruggeman rule (Ossenkopf 1991):

$$\sum_k f^k \frac{\varepsilon^k - \varepsilon_{\text{eff}}}{\varepsilon^k + 2\varepsilon_{\text{eff}}} = 0 \tag{13}$$

The grain emissivities, $E_\lambda^{[i]}(\lambda, a)$, were calculated by using the thermal-discrete approximation (TDA) to the general statistical-mechanical approach developed by Draine & Li (2001). The authors have shown that the TDA is quite good for calculating the overall emission spectrum of very small grains of typical sizes less than about 200 Å that experience temperature spikes. For larger grains, the grain emissivity can be easily calculated by using Planck function with the equilibrium grain temperature.

To calculate the energy balance of interstellar dust grains, we assume that the dust grains are heated by absorption of photons from the interstellar radiation field (ISRF) and are cooled via their own emission. The ISRF is defined by its mean intensity $J_\lambda^{\text{ISRF}}(\lambda)$. We adopted the empirical representation of $J_\lambda^{\text{ISRF}}(\lambda)$ for the solar neighborhood from Mathis et

al. (1983)

$$J_\lambda^{\mathrm{ISRF}}(\lambda) = J_\lambda^{\mathrm{UV}}(\lambda) + \sum_{j=1}^{3} W_j\, B_\lambda(\lambda, T_j) + B_\lambda(\lambda, T_{\mathrm{b}}), \qquad (14)$$

which includes the UV component, $J_\lambda^{\mathrm{UV}}(\lambda)$, three effective blackbody sources with dilution factors: $W_1=10^{-14}$, $W_2=10^{-13}$, $W_3=4\times10^{-13}$, and temperatures: $T_1=7500$ K, $T_2=4000$ K, $T_3=3000$ K, and the cosmic microwave background radiation, $B_\lambda(\lambda, T_{\mathrm{b}})$ with its temperature $T_{\mathrm{b}}=2.73$ K (Mather et al. 1994).

3. THE METHOD OF SOLUTION: REGULARIZATION

Equation (8) is a Fredholm integral equation of first kind, and its solution is a typical ill-posed inverse problem (Tikhonov et al. 1995). The inversion entails solving for the size distribution function $F(a)$ given a set of observations $D(x)$ and a kernel $K(x, a)$ which is calculated using an adopted grain model. As a rule, applying a kernel K to a function F is a smoothing operation. Consequently, the solution can be extremely sensitive to small changes in input data. Many specialized tools have been developed to tackle ill-posed equations. They utilize a priori information about the solution, such as its continuity, positivity, monotonic behavior, convexity, points of extremum, to name a few. Most popular are the method of regularization (Press et al. 1992; Tikhonov et al. 1995), the Backus-Gilbert method (Backus & Gilbert 1970), and the maximum entropy method (MEM) (Narayan & Nityananda 1986, e.g.).

To solve our specific problem, equation (8), we prefer to use the method of regularization (MR) which requires minimum input information: the data $D(x)$, their uncertainties $\sigma(x)$, and a stabilizing functional. The stabilizing functional is additional input information. It does not assume a parametric form for the solution, but it does assume that the solution will have a certain smoothness to it. In this sense, the MR has an advantage over the MEM, which additionally requires a default solution. Like the stabilizing functional in the MR (see eq. 17 below), the default serves to find a stable solution in the MEM. However, as a rule, it is practically impossible to guess the default solution in our case, as we will see later in § 5. Thus, the solutions derived with the MEM are more biased than those derived with the MR.

The MEM was used for modeling of interstellar extinction and polarization by Kim, Martin, & Hendry (1994), Kim & Martin (1994, 1995, 1996). A power law with an exponential cutoff was used as a default solution in all these papers. The use of such a default was partly justified because the authors performed their calculations largely within the frame-

work of then-standard graphite-silicate model by Draine & Lee (1984) which postulates power law grain-size distributions for both components. However, there are still problems with the default even in this case. For example, it is not clear how to choose the value of the exponential cutoff parameters that regulate the larger grain-size distribution: figures 2 and 6 from Kim & Martin (1996) can best serve to demonstrate the problem. At the same time, Zubko (1997) and Zubko, Krełowski, & Wegner (1996, 1998) have shown that the MR can be successfully applied for modeling of both circumstellar and interstellar extinction. There is no need for any default solution. Since the essential details of our numerical implementation of MR have already been described elsewhere (Zubko 1997), here we present only the key features of the method.

In the regularization approach, it is strictly proved that solving the integral equation (8) is equivalent to minimization of the following smoothing functional (Tikhonov et al. 1995):

$$\Psi[F^{(\alpha)}(a)] = \Phi_d[F^{(\alpha)}(a)] + \alpha\Phi_s[F^{(\alpha)}(a)] \tag{15}$$

where the two parts are: (1) the discrepancy functional:

$$\Phi_d[F^{(\alpha)}(a)] = \frac{1}{n_D}\sum_{j=1}^{n_D}\left[\frac{\int K(x_j, a)F^{(\alpha)}(a)\,da - D(x_j)}{w(x_j)}\right]^2, \tag{16}$$

and (2) the Tikhonov's stabilizing functional or stabilizer:

$$\Phi_s[F^{(\alpha)}(a)] = \int\{[F^{(\alpha)}(a)]^2 + \beta\,[dF^{(\alpha)}(a)/da]^2\}\,da, \tag{17}$$

α is the parameter of regularization ($\alpha \geq 0$), β is a dimensional adjusting parameter ($\beta \geq 0$), and $w(x)$ is the weight function. n_D is the total number of data points to fit. In our case, it includes the numbers of points of the extinction curve and emission spectrum, plus 6 points of the abundance constraints (C, Si, O, Mg, Fe, N). Generally, functional $\Phi_s[F^{(\alpha)}(a)]$ is a measure of smoothness of the solution and can contain derivatives of higher orders. However, the practice shows that keeping specific form (17) with the first derivative is sufficient for solving most ill-posed problems reducing to integral equation (8) (Tikhonov et al. 1995). This is also the case for our present study. If we measure F in μm^{-1} H^{-1} and a in μm, then α is expessed in μm H^2, and β in μm^2. Normally, the weights of both contributors to (17) are chosen to be equal: $\beta=1$ (Tikhonov et al. 1995). We also adopted this approach.

The solution is given by $F^{(\alpha)}$ that iteratively minimizes Ψ for an α that satisfies the discrepancy rule:

$$\Phi_d[F^{(\alpha)}(a)] = \Phi_d[F^{(\alpha=0)}(a)] + \frac{1}{n_D}\sum_{j=1}^{n_D}\left[\frac{\sigma(x_j)}{w(x_j)}\right]^2 \tag{18}$$

Note that equation (18) for α is solved simultaneously with the minimization of Ψ. It has been proved that Φ_d is a monotonic function of α: the larger α the larger Φ_d (Tikhonov et al. 1995). Thus, there exists a single unique solution for both α and $F^{(\alpha)}(a)$.

In the original formulation of the regularization approach (Tikhonov et al. 1995), the weight function was set to $w(x)\equiv1$. This formulation was used in the previous papers on modeling of interstellar extinction by one of us (Zubko et al. 1996a, 1998). However, we experimented with various expressions of $w(x)$ and found out that the choice of $w(x)=\sigma(x)$ is much more suitable for simultaneous fitting of various data sets (in our case: extinction + emission + abundances), and especially those having the large dynamic range of values. With this choice of $w(x)$, the discrepancy functional Φ_d resembles (but does not coincide with) the reduced χ^2 function, and the discrepancy rule (18) reads:

$$\Phi_d[F^{(\alpha)}(a)] = \Phi_d[F^{(\alpha=0)}(a)] + 1 \tag{19}$$

The introduction of Tikhonov's stabilizer is decisive in finding a mathematically stable and unique solution, that is a well-behaved function that does not have wild oscillations or discontinuities. If we would try to minimize the discrepancy functional Φ_d itself, when the number of unknown parameters (the values of function F at some discrete grid of grain sizes) exceeds the number of measurements or observations n_D, we would not obtain a unique solution for F: the functional Φ_d is degenerate in this case. However, the smoothing functional Φ_s is always nondegenerate. This guarantees that the combined functional Ψ is nondegenerate in any case [see chapter 18.4 in Numerical Recipes (Press et al. 1992) for more details]. In addition, because the functional Ψ is a strongly convex one (Tikhonov et al. 1995), minimization of Ψ will lead to a stable and unique solution for F. It results in some smoothing of the solution, and the extent of the smoothing, which is expressed by the parameter of regularization α, is defined by using the uncertainties $\sigma(x)$ through the discrepancy rule (19).

To minimize the smoothing functional Ψ, we use the iterative technique of conjugate gradient projections on nonnegative vector set, described in detail by Tikhonov et al. (1995). This provides even more stability to the solution, because the oscillations with changing sign are a priori excluded.

To estimate the uncertainty of the solution, we used the Monte Carlo-like computer simulation. Input observational data: extinction, emission, and elemental abundances have been perturbed by Gaussian noise with a standard deviation equal to the errors of the observations. By using the 'new' observational data, we calculated the grain-size distributions with the procedure described above. The variance of our results have been evaluated using an ensemble of such distributions. For the models reported here, we used the ensemble of

100 size distributions. We also experimented with larger ensembles of 500 and 1000 size distributions, but found that the variance in these cases is mostly similar to that for the case of 100 distributions.

In the discrepancy rule (eq. 18), the functional $\Phi_d[F^{(\alpha)}]$ is calculated for function $F^{(\alpha)}$ corresponding to the parameter of regularization α, whereas $\Phi_d[F^{(\alpha=0)}]$ is the minimum value of Φ_d corresponding to the case of no regularization: $\alpha = 0$. Generally, rule (18) is valid for an incompatible problem (eq. 8) which has no exact solution: $\Phi_d[F^{(\alpha=0)}] \neq 0$. This is the case for the models reported here.

4. MODELING DETAILS

4.1. Classes of Dust Models

We have fit the observational constraints with five different dust compositions, from which we created five different classes of dust models. The five different dust constituents are: (1) PAHs; (2) graphite; (3) amorphous carbon of types ACAR, BE, and ACH2; (4) silicates, $MgFeSiO_4$; and (5) composite particles containing different proportions of silicates, organic refractory material ($C_{25}H_{25}O_5N$), water ice (H_2O), and voids.

These five dust compositions were combined to create five different classes of dust models. The first class consists of PAHs, and bare graphite and silicate grains, identical to the carbonaceous/silicate model recently proposed by Li & Draine (2001b). The second class of models contains in addition to PAHs, bare graphite and silicate grains, composite particles. The third and fourth classes of models comprise of the first and second classes but with the graphite grains completely replaced by amorphous carbon grains. In the fifth class of models the only carbon is in PAHs, that is, it comprises of only PAHs, bare silicate, and composite particles.

We designated models including only PAHs and bare grains as BARE, and those containing additional composite particles as COMP. The BARE and COMP models were further subdivided according to the composition of the bare carbon particles used in the model: graphite, amorphous carbon, and no carbon, designated respectively by -GR, -AC, and -NC. For all model classes, we performed the fit using the three different sets of ISM abundances listed in Table 1: solar, B stars, and F and G stars (correspondingly designated as -S, -B, and -FG submodels). So, for example, a BARE model with graphite grains derived by assuming the solar ISM abundances is designated as BARE-GR-S, or a COMP model with no carbon obtained by assuming the B star abundances is designated as COMP-NC-B.

4.2. Computational Details

For computational purposes, we used a discrete set of wavelengths to calculate $D(x)$: a set of 100 wavelengths equally spaced in λ^{-1} between $1/3.0$ and $1/0.912$ μm^{-1} to characterize the extinction; eight wavelengths at 3.5, 4.9, 12, 25, 60, 100, 140, and 240 μm, corresponding to the nominal wavelengths of the DIRBE filters, and 93 wavelengths between 160 and 1000 μm, corresponding to the FIRAS channels, to characterize the IR emission. For each dust component, we constructed a grid of 30–100 grain radii, logarithmically distributed between a_{min} and a_{max}. We adopted a_{min}=3.5 Å for PAHs, graphite, and silicate grains, because smaller grains are photolytically unstable (Guhathakurta & Draine 1989). For composite grains, we performed calculations for larger values of a_{min}=100–500 Å, since composite grains, being aggregates of smaller particles, are a priori expected to be larger. For the composite grains the results do not depend drastically on a_{min}, so we adopted a_{min}=200 Å for these particles. Note that for the grains of sizes larger than 200 Å, the contribution of temperature fluctuations to the grain energy balance becomes negligible, and we can use the equilibrium temperature approach for calculating the emissivity of the grains. For all components, we chose the upper limit a_{max}=5 μm, but found that the size distribution is essentially zero for $a > 1$ μm for all the models even with a_{max} up to 20–50 μm.

5. RESULTS

5.1. Comparison with Constraints

The main results of our modeling are shown in Figures 4–18 which compare the calculations for the BARE and COMP models to the observations. Each figure consists of four panels depicting the following results: (1) the grain-size distributions and their uncertainties for each dust component, which is the main result of the fitting (inversion); (2) the calculated extinction curve, with the partial contributions of each dust component; (3) the calculated abundances of the different elements in the dust; and (4) the calculated emission spectrum along with the contributions of each dust component.

For BARE models with graphite grains, the main contribution to the UV/optical extinction comes from graphite grains and PAHs, whereas silicate grains dominate in the far UV extinction. The UV bump is explained by both PAHs and graphite grains. In emission, PAHs and graphite grains mostly contribute in the near infrared (3–25 μm), graphite grains prevail for λ=25–250 μm, and the contributions of graphite and silicate grains are comparable for $\lambda > 250$ μm.

For BARE models with amorphous carbon, most optical and UV extinction is explained by amorphous carbon grains: this contribution is quite flat. The far UV slope is provided by small silicate grains and PAHs. The UV bump is solely explained by PAHs. The near infrared emission is due to PAHs and silicate grains, the middle infrared ($\lambda=25$–60 μm) is explained by silicate grains, and the amorphous carbon grains prevail in the far infrared emission for $\lambda > 60$ μm.

COMP models with both graphite and amorphous carbon grains have some similarities with the respective BARE models. Note however that the composites are one of the main contributors to the optical to far-UV extinction. Emission in the near and mid infrared (3–60 μm) is similar to BARE models. However, composites contribute to emission in the far infrared for $\lambda > 200$ μm.

For COMP models without graphite or amorphous carbon grains, composites are dominating contributor to the infrared/optical/UV extinction and far infrared emission. The UV bump is explained by PAHs. These models generally require less carbon than any other models.

Figure 19 presents the size distribution for the BARE-GR-S dust model that comprises of dust particles with identical compositions and optical properties as the Li & Draine (2001b) model. For sake of comparison we also added in the figure the Li & Draine grain size distributions. For carbonaceous grains, the Li & Draine size distribution is tri-modal with a primary peak at around 0.3 μm, and secondary peaks at about 50 and 5 Å.

In contrast, our size distribution for the carbonaceous particles is bi-modal, consisting of a graphitic component peaked at $\sim$0.1 μm, and a PAH component, peaked at $\sim$15 Å. The graphitic component extends to very small grain sizes, representing a population of dehydrated PAHs. The dehydrated PAHs are needed to produce the continuum mid-IR emission without the associated PAH features. This mid-IR emission also masks the presence of the 10 μm silicate bump that is generated by the very small silicate particles in the BARE-GR-S dust model. The additional $\sim$50 Å bump at the lower limit of the Li & Draine graphite grain size distribution may reflect the need to produce a featureless mid-IR continuum emission in their model.

The silicate grain size distribution in both, the Li-Draine and the BARE-GR-S dust models, is essentially a power law with a similar cutoff at large grain sizes. However, the silicate size distribution in the BARE-GR-S model has a shallower slope, similar to that of the MRN model, and consequently contains a larger number of very small silicate particles compared to the Li-Draine model.

Another contribution to the differences in the grain size distribution between the BARE-

GR-S and the Li & Draine dust models may be attributed to the fact that Li & Draine (2001b) constrained the functional form of their size distributions, and thus did not derive the optimal distributions that fits the observational constraints.

When trying to find the best-fit COMP models, we varied the volume fractions of composite grains, including their porosities, to get the mimimum discrepancy. This resulted in a composite model which has *mass* fractions: 0.5 of silicate, 0.457 of organic refractory, and 0.043 of water ice, but with different porosities listed for each model in Table 4. In most cases, the models for a range of porosities 0.20–0.80 can provide quite good fits. So, for these cases, we present models for a porosity equal to 0.50, with two exceptions: (1) for COMP-AC-S, the models fits are good for porosities 0.50–0.70, so we chose the model with 0.60 as a representative; (2) for COMP-GR-B, the models with porosities 0–0.20 looks better, so we present a model with 0.10. We included various types of amorphous carbon in composites while modeling, but we found that in order to get good fits the mass fraction of amorphous carbon should not exceed 1%. Figure 20 demonstrates the optical constants for the composites with porosity 0.50, derived with the three various mixing rules. Also shown are the optical constants of the composite constituents: silicate, organic refractory, and water ice.

5.2. Quality of Fit

Table 3 lists the discrepancies of the models. It is immediately clear from the Table that the overall quality of models is highly dependent on the abundance constraint. The minimum discrepancy is achieved by the group of models that assume F and G stars ISM abundances with the models assuming solar and B star abundances following next. Note that the differences are quite small between the minimum and maximum discrepancies of neighboring groups of models with various abundances, that is between BARE-AC-FG and COMP-GR-S, and between BARE-AC-S and COMP-GR-B. The discrepancies for our models are within the range of 10±2. The amorphous carbon in the models listed in the table consist of ACH2 type carbon. We found that it is impossible to get acceptable fits with ACAR or BE type carbon.

Generally, each of the models provides acceptable fits to the extinction and emission. Quantitatively, this can be seen from Table 3 by comparing the respective discrepancies. There are however differences in fitting the abundances in dust. First of all, the COMP models have smaller discrepancies (Φ_d) than their BARE counterparts. Probably, this is mostly because COMP models include one more dust component – composites, and thus more fitting parameters. Even the models with the B stars abundances can provide acceptable fits

to the abundances in dust, while still requiring extra carbon beyond one sigma. By comparing the discrepancies from Table 3, we can conclude that it is harder to fit B star abundance constraints than the two other sets. Note however that larger abundance uncertainties for F and G stars make it easier to get good fits for this case. The COMP models provide somewhat better fits than their respective BARE counterparts.

Li & Draine (2001b) adopted an extinction-per-H-atom value that is 1.12 larger than that of our paper. However, this difference does not account for the large amount of metals consumed in their dust model, because the model was derived by fitting *both* the extinction and the emission spectrum. As a result, the abundance of the dust does not scale simply with the extinction curve. To examine the effect of the extinction curve on the elemental depletions, we calculated the dust abundances for a BARE-GR-S model optimized to fit the extinction curve used by Li & Draine (2001b) instead of the one used in this paper. The changes in the dust abundances were quite small, 2.6 and 0.9% for carbon and silicate dust, respectively. From this experiment we expect that a Li & Draine model fit to the extinction curve used here, will not substantially alter their derived dust abundances.

5.3. Characterization of the Models

5.3.1. Dust Abundances and Size Distributions

In Table 5, we list the quantities of chemical elements, consumed by the models: both total and partial for each dust component. Table 6 contains the dust-to-gas ratios and the mass per H atom locked up in dust along with the contributions of each dust constituent in per cent.

From the masses per H atom and the constituent mass percentages from Table 6, one can calculate the abundances of water ice required by our models. We found that our COMP models consume 5–13 ppm of ice (5–7 for COMP-GR models, 7–11 for COMP-AC models, and 12–13 for COMP-NC models). For comparison, Whittet et al. (1997) estimated the upper limit for water ice at the diffuse sightline toward Cygnus OB2 No. 12 to be 2 ppm. However, it is not clear whether this estimate is applicable to other diffuse lines of sight. On the other hand, Figure 21 (see §5.3.2) demonstrates that the near-infrared extinction predicted by our COMP models, especially at the wavelengths around the 3.1 and 6 μm water ice absorption features, is consistent with the observations for a line of sight toward the Galactic Center (Lutz et al. 1996).

We performed analytical approximations for the size distributions of all our models. At first step, the size distribution function $f(a)$ (in μm^{-1} H^{-1}) found in a numerical form was

expressed as $f(a) = A\,g(a)$, where A is a normalization coefficient in H^{-1}, a is in μm, and function $g(a)$ (in μm^{-1}) has a property $\int g(a)\,da = 1$. To analytically approximate numerical values of $g(a)$, we used function $\overline{g}$:

$$\log \overline{g}(a) = c_0 + b_0 \log(a) - b_1 \left| \log \left(\frac{a}{a_1} \right) \right|^{m_1} - b_2 \left| \log \left(\frac{a}{a_2} \right) \right|^{m_2} - b_3 |a - a_3|^{m_3} - b_4 |a - a_4|^{m_4} \quad (20)$$

which contains 14 parameters. Note this is a generic expression: we normally used 8–11 parameters for fitting. The parameters of $\overline{g}(a)$ were derived by fitting the numerical values of $g(a)$ using the nonlinear least-squares Marquardt-Levenberg algorithm (Press et al. 1992). Function (20) contains a power law part: $c_0 + b_0 \log(a)$, cutoff terms: $-b_i \left| \log(a/a_i) \right|^{m_i}$, and peaked terms: $-b_i |a - a_i|^{m_i}$. The cutoff and peaked terms are needed to reproduce the deviations of the model size distributions from a power law.

The resulting values of the parameters of the fitting function (20) are listed in Tables 7–21. The Tables also contain parameters a_{min} and a_{max} which define the range of grain radii for which the approximation is valid, the normalization constant A, and the reduced χ^2 characterizing the quality of the analytical approximation. Note that χ^2_{red} has no relation to the quality of the grain-size distribution model. Most approximations have χ^2_{red} better than of 0.01.

5.3.2. Near–Infrared Extinction, Albedo, and Asymmetry Parameter

Figure 21, shows the near-infrared extinction curves for the different BARE and COMP models. The observed extinction was taken from Lutz et al. (1996) who estimated it by using the hydrogen recombination lines detected between 2.5 and 9 μm towards the Galactic Center. Generally, the COMP models are more consistent with the observed extinction here: the features at around 3–3.5 and 5.5–7.0 μm are mostly due to water ice and organic refractory. It is immediately clear from Figure 21 that additional dust components should be present, e.g., other types of silicates, metal oxides or sulphides, CO_2 and methane ices; or else the optical constants for the existing components are bad. However, currently, it is impossible to involve these species into analysis because of lack of the respective optical constants. Note also that the Galactic Center line of sight may be very different from the high latitude emission and extinction that were fit, especially with regard to molecular clouds and thus probably composite or multilayer grains.

In Figures 22–23, we show the scattering properties of our dust models: the albedo, that is the ratio of the mean scattering cross section to the mean extinction cross section; and phase function asymmetry parameter which is the mean value of the cosine of the scattering angle. Generally, our models give slightly lower values than the observed ones,

but the COMP models look preferable in comparison to the BARE models, especially for the asymmetry parameter.

6. ASTROPHYSICAL IMPLICATIONS

An important result of our modeling is that the current extinction, IR emission, and interstellar abundance constraints can be simultaneously fit by several different classes of dust models.

One class of models consist of the widely-used PAH, bare graphite and silicate grains. With our addition of the abundance constraints we derive a similar carbon abundance in PAHs and graphite as Li & Draine (2001b) did, but with generally smaller graphite grains and larger PAH molecules (see Fig. 19). Our silicate size distribution turns out to be similar to the MRN distribution, with a shallower slope than the Li & Draine model. The peak in our silicate grain size distribution is lower than that in their model, which is why our Mg/H, Si/H, and Fe/H abundance in the dust is only 33 ppm, compared to the ≈ 50 required in the Li & Draine model.

A second class of dust models that fits the constraints contains in addition to bare grains, composite particles, such as those believed to have formed and observed to be present in dense molecular clouds (Greenberg & Li 1999; Tielens et al. 1996; Schutte et al. 1998; Chiar et al. 2000, e.g.). The sizes of the composite particles are generally larger than those of the bare particles. This is consistent with the scenario in which the ices and organic material of the composite grains accumulated in molecular clouds, producing larger dust aggregates than expected in the diffuse ISM. The presence of such particles in the diffuse ISM would imply that their volatile components survive the harsher radiation field in that environment. This may be due to the fact that the volatile compounds may have accreted in protected areas of the dust particles, that the large size of the composite grains prevents surges in their temperature which would evaporate the volatiles, and that the volatiles may have been reprocessed by UV radiation into a more refractory component. In our future works, we hope to include other volatile materials, e.g. icy methane, ammonia, carbon dioxide, and other oxides, when the respective optical constants are measured in laboratory.

We also presented a class of BARE and COMP models in which graphite is completely replaced by hydrogenated amorphous carbon. In these models, PAHs are the only contributor to the UV extinction bump at 2175 Å. These models are motivated by the fact that the highly ordered structure of graphite is unlikely to form in circumstellar environments, and survive in the diffuse ISM, making amorphous carbon grains more atractive alternative

(Witt 2000). We note that the discrepancies of models containing amorphous carbon are generally larger than those containing graphite, which may be due to the fact that their optical constants were not optimized to fit astronomical observations. In contrast, the optical constants for "astronomical" graphite and "astronomical" silicate used in this study have been basically derived by Draine & Lee (1984) by fitting laboratory measurements and interstellar extinction law, using the MRN model of graphite and silicate grains with a power-law size distribution. So, it should not be surprising that dust models without graphite will not provide as good a fit as those that do.

A final class of models contains no carbon at all, except for that present in PAHs, and in the organic constituent of the composite particles. This model was motivated by the desire to fit the lowest available carbon abundance in dust if the ISM had B star abundances. The model, designated COMP-NC-B, consumes less carbon, $C/H \approx 196$ ppm, compared to models COMP-GR-B ($C/H \approx 240$ ppm) or COMP-AC-B ($C/H \approx 207$ ppm) (Table 5). This class of models is made possible by the fact that the absorption cross sections of a mixture of "astronomical" PAHs were adjusted by Li & Draine (2001b) to fit the UV extinction bump at 2175 Å. These are idealized cross sections which ignore substructures in the measured UV absorption of the PAH mixtures (Léger et al. 1989; Joblin, Léger, & Martin 1992).

Since several classes of dust models fit the observed extinction, IR emission, and elemental abundances, any linear combination of these models will provide equally good fits to these constraints. This provides a wide range of latitude in the construction of evolutionary models in which dust cycles between the various ISM phases, allowing for spatial variations in dust composition and size distribution in the diffuse ISM without significantly affecting the average extinction.

7. CONCLUSIONS

We have taken an additional step in the characterization of interstellar dust particles, by simultaneopusly fitting their interstellar extinction, diffuse IR emission, and interstellar abundance constraints. We used dust constituents with physical optical constants and properties to characterize the components of the dust model: PAHs, silicates, graphite, amorphous carbon, and composite particles. Given the observational constraints and the dust consituents and properties, we used the method of regularization to solve for the optimal grain size distribution of each dust component.

The principal results of this paper are as follows:

1. We found that bare grain (BARE) models (PAHs + graphite + silicate or PAHs +

amorphous carbon + silicate) provide good simultaneous fits to the far-UV to near-IR extinction, thermal IR emission, and elemental abundance constraints.

2. Somewhat improved fits to the observational constraints are obtained by the composite grain (COMP) models, through the addition of composite grains (silicate + organic refractory + water ice + voids) to the bare grain model.

3. The COMP-GR-FG model provides the best fit to the extinction and IR emission if the ISM has F and G stars abundances. The model also provides a good match to the observed infrared extinction and scattering properties: albedo and asymmetry parameter.

4. The results of our calculations show that it is harder to fit the B star abundances than the solar or F and G star abundances. Thus, we can conclude that solar or F and G star abundances for diffuse interstellar medium look preferable.

5. The results of our modeling demonstrate that there is no unique dust model that fits the extinction, IR emission, and elemental abundances constraints. We believe that adding more constraints, such as interstellar polarization could narrow the set of viable dust models.

6. Preliminary calculations show that haloes produced by small angle X-ray scattering can discriminate between the different dust models, favoring BARE over COMP models, which have a larger population of big particles (Dwek et al. 2004).

REFERENCES

Allamandola, L.J., Tielens, A.G.G.M., & Barker, J.R. 1985, ApJ, 290, L25

Arendt, R.G., et al. 1998, ApJ, 508, 74

Backus, G.E., & Gilbert, F. 1970, Geophysical Journal of the Royal Astronomical Society, 16, 169

Bohlin, F.C., Savage, B.D., & Drake, J.F. 1978, ApJ, 224, 132

Bohren, C.F., & Huffman, D.R. 1983, Absorption and Scattering of Light by Small Particles (New York: Wiley-Interscience)

Cardelli, J.A., Clayton, G.C., Mathis, J.S. 1989, ApJ, 345, 245

Cardelli, J.A., Meyer, D.M., Jura, M., & Savage, B.D. 1996, ApJ, 467, 334

Chiar, J.E., Tielens, A.G.G.M., Whittet, D.C.B., Schutte, W.A., Boogert, A.C.A., Lutz, D., van Dishoeck, E.F., & Bernstein, M.P. 2000, ApJ, 537, 749

Colangeli, L., Mennella, V., Palumbo, P., Rotundi, A., Bussoletti, E. 1995, A&AS, 113, 561

Désert, F.X., Boulanger, F., & Puget, J.L. 1990, A&A, 237, 215

Draine, B.T. 1989, in Infrared Spetroscopy in Astronomy, ed. B.H. Kaldeich (Paris: ESA), 93

Draine, B.T., & Lee, H.M. 1984, ApJ, 285, 89

Draine, B.T., & Anderson, N. 1985, ApJ, 292, 494

Draine, B.T., & Li, A. 2001, ApJ, 551, 807

Dwek, E., et al. 1997, ApJ, 475, 565

Dwek, E., Zubko, V., Arendt, R. G., & Smith, R. K. 2004, in ASP Conference Series Vol. 000, eds. A.N. Witt, B.T. Draine, & G.C. Clayton (San Francisco: ASP), page 000

Fitzpatrick, E.L. 1999, PASP, 111, 63

Greenberg, J.M. 1968, in Stars and Stellar Systems, Vol. 7, ed. B.M. Middlehurst & L.H. Aller (Chicago: Univ. of Chicago Press), 221

Greenberg, J.M., & Li, A. 1999, Adv. Space Res., 24, 497

Guhathakurta, P. & Draine, B.T. 1989, ApJ, 345, 230

Holweger, H. 2001, in Joint SOHO/ACE workshop "Solar and Galactic Composition", ed. R.F. Wimmer-Schweingruber, American Institute of Physics Conference proceedings, vol. 598, p.23

Joblin, C., Léger, A., & Martin, P. 1992, ApJ, 393, L79

Kim, S.-H., & Martin, P.G., 1994, ApJ, 431, 783

Kim, S.-H., & Martin, P.G., 1995, ApJ, 444, 293

Kim, S.-H., & Martin, P.G., 1996, ApJ, 462, 296

Kim, S.-H., Martin, P.G., & Hendry, P.D. 1994, ApJ, 422, 164

Laor, A., & Draine, B.T. 1993, ApJ, 402, 441

Léger, A., & Puget, J.L. 1984, A&A, 137, 5L

Léger, A., Verstraete, L., d'Hendecourt, L., Défourneau, D., Dutuit, O., Schmidt, W., & Lauer, J. 1989, in IAU Symp. 135, Interstellar Dust, ed. L.J. Allamandola & A.G.G.M. Tielens (Dordrecht: Kluwer), 173

Lehtinen, K., & Mattila, K. 1996, A&A, 309, 570

Li, A., & Draine, B.T. 2001, ApJ, 550, L213

Li, A., & Draine, B.T. 2001, ApJ, 554, 778

Li, A., & Greenberg, J.M. 1997, A&A, 323, 566

Lillie, C.F., & Witt, A.N. 1976, ApJ, 208, 64

Lutz, D., et al. 1996, A&A, 315, L269

Mather, J.C., et al. 1994, ApJ, 420, 439

Mathis, J.S., Rumpl, W., & Nordsieck, K.H. 1977, ApJ, 217, 425 (MRN)

Mathis, J.S., Mezger, P.G., & Panagia, N. 1983, A&A, 128, 212

Meyer, D.M., Cardelli, J.A., & Sofia, U.J. 1997, ApJ, 490, L103

Meyer, D.M., Jura, M., & Cardelli, J.A. 1998, ApJ, 493, 222

Morgan, D.H., Nandy, K., & Thompson, G.I. 1976, MNRAS, 177, 531

Narayan, R., & Nityananda, R. 1986, ARA&A, 24, 127

Ossenkopf, V. 1991, A&A, 251, 210

Press, W.H., Teukolsky, S.A., Vetterling, W.T., & Flannery, B.P. 1992, Numerical Recipes in C: The Art of Scientific Computing. Second Edition (Cambridge University Press)

Sasseen, T.P., Hurwitz, M., Dixon, W.V., & Airieau, S. 2002, ApJ, 566, 267

Savage, B.D., & Mathis, J.S. 1979, ARA&A, 17, 73

Savage, B.D., Massa, D.L., Meade, M., & Wesselius, P.R., 1985, ApJS, 59, 397

Schutte, W.A., et al. 1998, A&A, 337, 261

Snow, T.P., & Witt, A.N. 1996, ApJ, 468, L65

Sofia, U.J., & Meyer, D.M. 2001, ApJ, 554, L221

Stognienko, R., Henning, Th., & Ossenkopf, V. 1995, A&A, 296, 797

Tielens, A.G.G.M., Wooden, D.H., Allamandola, L.J., Brigman, J., & Witteborn, F.C. 1996, ApJ, 461, 210

Tikhonov, A.N., Goncharsky, A.V., Stepanov, V.V., & Yagola, A. 1995, Numerical Methods for the Solution of Ill-Posed Problems (Dordrecht, the Netherlands: Kluwer Academic Publishers)

Tokunaga, A. T. 1997, in "Diffuse Infrared radiation and the IRTS", eds. H. Okuda, T. Matsumoto, and T. L. Roellig (A.S.P.; san Francisco), p. 149

Warren, S.G. 1984, Appl. Opt., 23, 1206

Weingartner, J.C., & Draine, B.T. 2001, ApJ, 548, 296

Whittet, D.C.B., et al. 1997, ApJ, 490, 729

Witt, A.N. 1989, in IAU Symp. 135, Interstellar Dust, ed. L.J. Allamandola & A.G.G.M. Tielens (Dordrecht: Reidel), 87

Witt, A. N. 2000, in IAU Symp. 197, Astrochemistry: From Molecular Clouds to Planetary Systems, ed. Y.C. Minh & E.F. van Dishoeck (San Francisco: ASP), 317

Witt, A.N., Friedmann, B.C., & Sasseen, T.P. 1997, ApJ, 481, 809

Zubko, V.G. 1997, MNRAS, 289, 305

Zubko, V.G., Krełowski, J., & Wegner, W. 1996, MNRAS, 283, 577

Zubko, V.G., Krełowski, J., & Wegner, W. 1998, MNRAS, 294, 548

Zubko, V.G., Mennella, V., Colangeli, L., & Bussoletti, E. 1996, MNRAS, 282, 1321

Table 1. Inferred Dust Phase Abundances In the Diffuse ISM per 10^6 H Atoms.

		C	O	Si	Mg	Fe	N
Total ISM	Solar[a]	391±98	545±100	34.4±3.9	34.5±4.8	28.1±5.4	85.2±21.9
	F & G Stars[b]	358±82	445±156	39.9±13.1	42.7±17.2	27.9±7.7	$\cdots$
	B Stars[b]	190±77	350±133	18.8±8.9	23.0±7.0	28.5±18.0	64.7±34.2
Gas Phase[c]		108±16	319±14	≈ 0	≈ 0	≈ 0	75.0±4.0
Dust Phase	Solar (S)	283±99	226±101	34.4±3.9	34.5±4.8	28.1±5.4	10.2±22.3
	F & G Stars (FG)	250±84	126±157	39.9±13.1	42.7±17.2	27.9±7.7	$\cdots$
	B Stars (B)	82±79	31±134	18.8±8.9	23.0±7.0	28.5±18.0	0.0±35

[a]Holweger (2001)

[b]Sofia & Meyer (2001)

[c] The value for C is a straight average of two available estimates of 140±20 by Cardelli et al. (1996) and 75±25 by Dwek et al. (1997); the values for O and N are from Meyer et al. (1998) and Meyer et al. (1997), respectively

Table 2.   Properties of dust constituents.

Constituent	Composition	Mass density g cm^{-3}	Optical constants References
PAHs	C	2.24	Li & Draine 2001b
Graphite	C	2.24	Laor & Draine 1993
Silicate	MgFeSiO$_4$	3.5	Weingartner & Draine 2001
Amorphous Carbon	C	1.81–1.87	Zubko et al. 1996
Organic Refractory	C$_{25}$H$_{25}$O$_5$N	1.6	Li & Greenberg 1997
Water Ice	H$_2$O	0.92	Warren 1984

Table 3.   Discrepancies of the dust models.

Model	Φ_d	Φ_d^{ext}	Φ_d^{emis}	Φ_d^{abund}	α
COMP-GR-FG	8.22	0.09	7.91	0.22	0.828
BARE-GR-FG	8.38	0.14	8.03	0.21	0.859
COMP-AC-FG	8.44	0.12	8.07	0.25	0.283
COMP-NC-FG	8.48	0.12	8.02	0.34	0.278
BARE-AC-FG	9.07	0.30	8.54	0.23	0.300
COMP-GR-S	9.27	0.10	8.82	0.35	1.106
COMP-AC-S	9.46	0.14	8.98	0.34	0.325
BARE-GR-S	9.48	0.17	8.93	0.38	1.123
COMP-NC-S	9.51	0.14	8.99	0.38	0.322
BARE-AC-S	10.12	0.33	9.43	0.36	0.341
COMP-GR-B	10.42	0.20	9.21	1.01	1.233
COMP-AC-B	10.57	0.14	9.62	0.81	0.346
COMP-NC-B	10.58	0.14	9.67	0.77	0.349
BARE-GR-B	10.76	0.27	9.33	1.16	1.290
BARE-AC-B	11.72	0.47	9.87	1.38	0.360

Note. — The table lists the total discrepancies for the models, Φ_d, together with the contributions from extinction, Φ_d^{ext}, emission, Φ_d^{emis}, and abundances, Φ_d^{abund}. By definition: $\Phi_d = \Phi_d^{ext} + \Phi_d^{emis} + \Phi_d^{abund}$. The last column contains the parameter of regularization, α, in μm H^2.

Table 4.   Volume fractions of constituents and average mass densities of model composite particles.

Model	Voids	Silicate	Organic Refractory	Water Ice	Density (g cm^{-3})
COMP-GR-S	0.50	0.15	0.30	0.05	1.05
COMP-AC-S	0.60	0.12	0.24	0.04	0.84
COMP-NC-S	0.50	0.15	0.30	0.05	1.05
COMP-GR-FG	0.50	0.15	0.30	0.05	1.05
COMP-AC-FG	0.50	0.15	0.30	0.05	1.05
COMP-NC-FG	0.50	0.15	0.30	0.05	1.05
COMP-GR-B	0.10	0.27	0.54	0.09	1.89
COMP-AC-B	0.50	0.15	0.30	0.05	1.05
COMP-NC-B	0.50	0.15	0.30	0.05	1.05

Table 5.   Atomic abundances in dust in atoms per 10^6 H Atoms for various models.

Model	Component	C	O	Si	Mg	Fe	N
BARE-GR-S	*Total*	*245.9*	*133.2*	*33.3*	*33.3*	*33.3*	*0.0*
	PAHs	33.0	0.0	0.0	0.0	0.0	0.0
	Graphite	212.9	0.0	0.0	0.0	0.0	0.0
	Silicate	0.0	133.2	33.3	33.3	33.3	0.0
BARE-GR-FG	*Total*	*247.5*	*132.4*	*33.1*	*33.1*	*33.1*	*0.0*
	PAHs	35.2	0.0	0.0	0.0	0.0	0.0
	Graphite	212.3	0.0	0.0	0.0	0.0	0.0
	Silicate	0.0	132.4	33.1	33.1	33.1	0.0
BARE-GR-B	*Total*	*254.4*	*114.0*	*28.5*	*28.5*	*28.5*	*0.0*
	PAHs	33.3	0.0	0.0	0.0	0.0	0.0
	Graphite	221.1	0.0	0.0	0.0	0.0	0.0
	Silicate	0.0	114.0	28.5	28.5	28.5	0.0
BARE-AC-S	*Total*	*265.0*	*134.0*	*33.5*	*33.5*	*33.5*	*0.0*
	PAHs	51.4	0.0	0.0	0.0	0.0	0.0
	ACH2	213.6	0.0	0.0	0.0	0.0	0.0
	Silicate	0.0	134.0	33.5	33.5	33.5	0.0
BARE-AC-FG	*Total*	*265.1*	*136.8*	*34.2*	*34.2*	*34.2*	*0.0*
	PAHs	52.4	0.0	0.0	0.0	0.0	0.0
	ACH2	212.7	0.0	0.0	0.0	0.0	0.0
	Silicate	0.0	136.8	34.2	34.2	34.2	0.0
BARE-AC-B	*Total*	*275.3*	*114.8*	*28.7*	*28.7*	*28.7*	*0.0*
	PAHs	52.2	0.0	0.0	0.0	0.0	0.0
	ACH2	223.1	0.0	0.0	0.0	0.0	0.0
	Silicate	0.0	114.8	28.7	28.7	28.7	0.0
COMP-GR-S	*Total*	*217.4*	*153.6*	*33.0*	*33.0*	*33.0*	*3.0*
	PAHs	33.5	0.0	0.0	0.0	0.0	0.0
	Graphite	109.2	0.0	0.0	0.0	0.0	0.0
	Silicate	0.0	100.0	25.0	25.0	25.0	0.0
	Composites	74.7	53.6	8.0	8.0	8.0	3.0
COMP-GR-FG	*Total*	*227.9*	*146.7*	*32.4*	*32.4*	*32.4*	*2.4*
	PAHs	35.8	0.0	0.0	0.0	0.0	0.0
	Graphite	133.3	0.0	0.0	0.0	0.0	0.0
	Silicate	0.0	104.4	26.1	26.1	26.1	0.0
	Composites	58.8	42.3	6.3	6.3	6.3	2.4
COMP-GR-B	*Total*	*239.8*	*132.4*	*27.8*	*27.8*	*27.8*	*2.9*
	PAHs	33.7	0.0	0.0	0.0	0.0	0.0
	Graphite	133.0	0.0	0.0	0.0	0.0	0.0
	Silicate	0.0	80.0	20.0	20.0	20.0	0.0

Table 5—Continued

Model	Component	C	O	Si	Mg	Fe	N
	Composites	73.1	52.4	7.8	7.8	7.8	2.9
COMP-AC-S	*Total*	*216.7*	*159.7*	*33.3*	*33.3*	*33.3*	*3.6*
	PAHs	50.6	0.0	0.0	0.0	0.0	0.0
	ACH2	75.2	0.0	0.0	0.0	0.0	0.0
	Silicate	0.0	94.8	23.7	23.7	23.7	0.0
	Composites	90.9	64.9	9.6	9.6	9.6	3.6
COMP-AC-FG	*Total*	*219.3*	*160.0*	*33.8*	*33.8*	*33.8*	*3.5*
	PAHs	51.7	0.0	0.0	0.0	0.0	0.0
	ACH2	81.2	0.0	0.0	0.0	0.0	0.0
	Silicate	0.0	98.0	24.5	24.5	24.5	0.0
	Composites	86.4	62.0	9.2	9.2	9.2	3.5
COMP-AC-B	*Total*	*206.9*	*148.5*	*27.9*	*27.9*	*27.9*	*5.1*
	PAHs	51.5	0.0	0.0	0.0	0.0	0.0
	ACH2	28.1	0.0	0.0	0.0	0.0	0.0
	Silicate	0.0	57.2	14.3	14.3	14.3	0.0
	Composites	127.3	91.3	13.6	13.6	13.6	5.1
COMP-NC-S	*Total*	*188.2*	*173.6*	*33.4*	*33.4*	*33.4*	*5.5*
	PAHs	50.0	0.0	0.0	0.0	0.0	0.0
	Silicate	0.0	74.8	18.7	18.7	18.7	0.0
	Composites	138.2	98.8	14.7	14.7	14.7	5.5
COMP-NC-FG	*Total*	*189.9*	*175.6*	*33.9*	*33.9*	*33.9*	*5.6*
	PAHs	51.0	0.0	0.0	0.0	0.0	0.0
	Silicate	0.0	76.4	19.1	19.1	19.1	0.0
	Composites	138.9	99.2	14.8	14.8	14.8	5.6
COMP-NC-B	*Total*	*196.1*	*154.3*	*28.1*	*28.1*	*28.1*	*5.8*
	PAHs	51.5	0.0	0.0	0.0	0.0	0.0
	Silicate	0.0	50.8	12.7	12.7	12.7	0.0
	Composites	144.6	103.5	15.4	15.4	15.4	5.8

Note. — The first column is a name of the model; next column lists the components for each model; next six columns are the numbers of elements in dust components in ppm. The total abundances summed up over all components are in italics.

Table 6.   Mass in dust for various models.

Model	dust/gas	M (g H^{-1})	PAHs	Graphite	ACH2	Silicate	Water Ice	Organics
Li & Draine 2001	0.00813	$1.89{\times}10^{-26}$	26.77		$\cdots$	73.23	$\cdots$	$\cdots$
BARE-GR-S	0.00619	$1.44{\times}10^{-26}$	4.57	29.47	$\cdots$	65.96	$\cdots$	$\cdots$
BARE-GR-FG	0.00618	$1.43{\times}10^{-26}$	4.88	29.44	$\cdots$	65.68	$\cdots$	$\cdots$
BARE-GR-B	0.00568	$1.32{\times}10^{-26}$	5.02	33.38	$\cdots$	61.60	$\cdots$	$\cdots$
BARE-AC-S	0.00639	$1.49{\times}10^{-26}$	6.89	$\cdots$	28.65	64.46	$\cdots$	$\cdots$
BARE-AC-FG	0.00648	$1.51{\times}10^{-26}$	6.94	$\cdots$	28.15	64.91	$\cdots$	$\cdots$
BARE-AC-B	0.00589	$1.37{\times}10^{-26}$	7.60	$\cdots$	32.47	59.93	$\cdots$	$\cdots$
COMP-GR-S	0.00626	$1.46{\times}10^{-26}$	4.59	14.96	$\cdots$	64.78	1.37	14.30
COMP-GR-FG	0.00620	$1.44{\times}10^{-26}$	4.94	18.43	$\cdots$	64.20	1.09	11.34
COMP-GR-B	0.00580	$1.35{\times}10^{-26}$	4.98	19.64	$\cdots$	58.86	1.44	15.08
COMP-AC-S	0.00637	$1.48{\times}10^{-26}$	6.81	$\cdots$	10.13	64.34	1.63	17.09
COMP-AC-FG	0.00642	$1.49{\times}10^{-26}$	6.90	$\cdots$	10.85	64.60	1.54	16.11
COMP-AC-B	0.00578	$1.34{\times}10^{-26}$	7.63	$\cdots$	4.16	59.31	2.53	26.37
COMP-NC-S	0.00635	$1.48{\times}10^{-26}$	6.76	$\cdots$	$\cdots$	64.68	2.49	26.07
COMP-NC-FG	0.00642	$1.49{\times}10^{-26}$	6.81	$\cdots$	$\cdots$	64.80	2.48	25.91
COMP-NC-B	0.00579	$1.35{\times}10^{-26}$	7.62	$\cdots$	$\cdots$	59.64	2.86	29.88

Note. — The first column is name of the model; next two columns contain the dust-to-gas mass ratio and the mass in dust per one H atom; the rest of columns are the contributions of dust constituents in the dust mass in per cent.

Table 7.   Parameters of the analytical approximations to the size distributions for the
BARE-GR-S model.

	PAHs	Graphite	Silicate
A	2.227433−7	1.905816−7	1.471288−7
$a_{\min}$	0.00035	0.00035	0.00035
$a_{\max}$	0.005	0.33	0.37
χ^2_{red}	1.57548−4	8.60041−2	4.40336−2
c_0	−8.02895	−9.86000	−8.47091
b_0	−3.45764	−5.02082	−3.68708
b_1	1.18396+3	5.81215−3	2.37316−5
a_1	1.0	0.415861	7.64943−3
m_1	−8.20551	4.63229	22.5489
b_2	$\cdots$	$\cdots$	$\cdots$
a_2	$\cdots$	$\cdots$	$\cdots$
m_2	$\cdots$	$\cdots$	$\cdots$
b_3	1.0+24	1.12502+3	2.96128+3
a_3	−5.29496−3	0.160344	0.480229
m_3	12.0146	3.69897	12.1717
b_4	$\cdots$	1.12602+3	$\cdots$
a_4	$\cdots$	0.160501	$\cdots$
m_4	$\cdots$	3.69967	$\cdots$

Note. — The size distribution function $f(a)$ (in $\mu\mathrm{m}^{-1}\ \mathrm{H}^{-1}$) found in a numerical form is expressed as $f(a) = A\, g(a)$, where A is a normalization coefficient in H^{-1}, a is in $\mu\mathrm{m}$, and function $g(a)$ (in $\mu\mathrm{m}^{-1}$) has a property $\int g(a)\, \mathrm{d}a = 1$. To analytically approximate numerical values of $g(a)$, we used a 14-parameter function $\overline{g}$: $\log \overline{g}(a) = c_0 + b_0 \log(a) - b_1 \left|\log\left(a/a_1\right)\right|^{m_1} - b_2 \left|\log\left(a/a_2\right)\right|^{m_2} - b_3|a - a_3|^{m_3} - b_4|a - a_4|^{m_4}$. Parameters $a_{\min}$ and $a_{\max}$, both in $\mu\mathrm{m}$, define the range of grain radii for which the approximations are valid. χ^2_{red} is the reduced χ^2 for the fit of the approximation to the model size distribution (not the fit of the model to the constraints).

Table 8.   Parameters of the analytical approximations to the size distributions for the BARE-GR-FG model.

	PAHs	Graphite	Silicate
A	$2.484404-7$	$1.901190-7$	$1.541199-7$
a_{min}	0.00035	0.00035	0.00035
a_{max}	0.005	0.3	0.34
χ^2_{red}	$2.18384-4$	$6.679-2$	$9.70614-2$
c_0	-8.54571	-10.1149	-8.53081
b_0	-3.60112	-5.3308	-3.70009
b_1	$1.86525+5$	$7.54276-2$	$3.96003-9$
a_1	1.0	$8.08703-2$	$9.11246-3$
m_1	-13.5755	3.37644	47.0606
b_2	$\cdots$	$\cdots$	$\cdots$
a_2	$\cdots$	$\cdots$	$\cdots$
m_2	$\cdots$	$\cdots$	$\cdots$
b_3	$1.0+24$	$1.12502+3$	$1.48+3$
a_3	$1.98119-3$	0.145378	0.484381
m_3	9.25894	3.49042	12.3253
b_4	$\cdots$	$1.12602+3$	$1.481+3$
a_4	$\cdots$	0.169079	0.474035
m_4	$\cdots$	3.63654	12.0995

Table 9.   Parameters of the analytical approximations to the size distributions for the BARE-GR-B model.

	PAHs	Graphite	Silicate
A	2.187355−7	1.879863−7	1.238052−7
$a_{\min}$	0.00035	0.00035	0.00035
$a_{\max}$	0.0055	0.32	0.32
χ^2_{red}	6.4061−4	0.165084	1.46712−2
c_0	−8.84618	−9.92887	−8.53419
b_0	−3.69582	−5.14159	−3.7579
b_1	1.23836+5	4.68489−3	3.89361−13
a_1	1.0	0.450668	1.27635−3
m_1	−13.5577	4.85266	34.0815
b_2	· · ·	· · ·	· · ·
a_2	· · ·	· · ·	· · ·
m_2	· · ·	· · ·	· · ·
b_3	1.0+24	1.12505+3	1.481+3
a_3	2.3281−3	0.154046	0.268976
m_3	9.36086	3.56481	13.3815
b_4	· · ·	1.12605+3	1.48003+3
a_4	· · ·	0.153688	0.836879
m_4	· · ·	3.56482	44.1634

Table 10. Parameters of the analytical approximations to the size distributions for the COMP-GR-S model.

	PAHs	Graphite	Silicate	Composites
A	$2.243145-7$	$1.965000-7$	$1.160677-7$	$6.975520-12$
$a_{\min}$	0.00035	0.00035	0.00035	0.02
$a_{\max}$	0.0055	0.5	0.44	0.9
χ^2_{red}	$8.24665-6$	$2.89125-3$	$2.70197-3$	$1.06335-3$
c_0	-8.97672	-10.4717	-5.77068	-3.90395
b_0	-3.73654	-5.32268	-3.82724	-3.5354
b_1	$9.86507+10$	$5.63787-3$	$1.4815-7$	$9.85176-31$
a_1	1.0	$7.75892-2$	$7.44945-3$	$2.30147-4$
m_1	-14.8506	3.33491	12.3238	33.3071
b_2	$\cdots$	$\cdots$	$\cdots$	$\cdots$
a_2	$\cdots$	$\cdots$	$\cdots$	$\cdots$
m_2	$\cdots$	$\cdots$	$\cdots$	$\cdots$
b_3	$1.0+24$	$1.12504+3$	5.843	$\cdots$
a_3	$2.34542-3$	0.125304	0.398924	$\cdots$
m_3	9.33589	6.04033	0.561698	$\cdots$
b_4	$\cdots$	$1.12597+3$	$\cdots$	$\cdots$
a_4	$\cdots$	0.271622	$\cdots$	$\cdots$
m_4	$\cdots$	4.67116	$\cdots$	$\cdots$

Table 11.   Parameters of the analytical approximations to the size distributions for the COMP-GR-FG model.

	PAHs	Graphite	Silicate	Composites
A	2.520814−7	1.936847−7	1.309292−7	5.393662−12
$a_{\min}$	0.00035	0.00035	0.00035	0.02
$a_{\max}$	0.005	0.39	0.39	0.75
χ^2_{red}	1.10438−5	5.57211−3	1.74117−2	1.11274−3
c_0	−8.72489	−11.1324	−3.81346	−3.82614
b_0	−3.65649	−6.6148	−3.76412	−3.48373
b_1	9.86507+10	3.66626−2	2.62792−9	9.86756−31
a_1	1.0	0.144398	7.26393−3	4.13811−4
m_1	−14.6651	2.54938	15.5036	34.9122
b_2	$\cdots$	$\cdots$	$\cdots$	$\cdots$
a_2	$\cdots$	$\cdots$	$\cdots$	$\cdots$
m_2	$\cdots$	$\cdots$	$\cdots$	$\cdots$
b_3	1.0+24	1.12501+3	6.64727	$\cdots$
a_3	2.05181−3	0.166373	0.344185	$\cdots$
m_3	9.20391	4.58796	0.21785	$\cdots$
b_4	$\cdots$	1.126+3	$\cdots$	$\cdots$
a_4	$\cdots$	0.400672	$\cdots$	$\cdots$
m_4	$\cdots$	6.14619	$\cdots$	$\cdots$

Table 12.   Parameters of the analytical approximations to the size distributions for the COMP-GR-B model.

	PAHs	Graphite	Silicate	Composites
A	2.216925$-$7	1.918716$-$7	1.082933$-$7	4.780856$-$12
a_{min}	0.00035	0.00035	0.00035	0.02
a_{max}	0.0055	0.52	0.33	0.45
χ^2_{red}	8.51192$-$6	5.39803$-$3	6.53544$-$4	2.64688$-$3
c_0	$-$9.04531	$-$10.1159	1.39336$+$2	$-$3.72463
b_0	$-$3.75834	$-$5.45055	$-$3.66338	$-$3.4173
b_1	9.86507$+$10	2.58749$-$3	2.85829$-$10	2.56334$-$26
a_1	1.0	9.91702$-$2	5.26352$-$3	2.05195$-$4
m_1	$-$14.9148	3.71707	16.487	29.4592
b_2	$\cdots$	$\cdots$	$\cdots$	$\cdots$
a_2	$\cdots$	$\cdots$	$\cdots$	$\cdots$
m_2	$\cdots$	$\cdots$	$\cdots$	$\cdots$
b_3	1.0$+$24	1.0023$+$2	1.48931$+$2	$\cdots$
a_3	2.38145$-$3	0.200689	0.341914	$\cdots$
m_3	9.34323	3.52158	5.05577$-$3	$\cdots$
b_4	$\cdots$	1.00027$+$2	$\cdots$	$\cdots$
a_4	$\cdots$	0.699922	$\cdots$	$\cdots$
m_4	$\cdots$	9.86403	$\cdots$	$\cdots$

Table 13. Parameters of the analytical approximations to the size distributions for the BARE-AC-S model.

	PAHs	ACH2	Silicate 1	Silicate 2
A	$4.492237-7$	$8.185937-12$	$3.527574-7$	$6.134893-13$
a_{min}	0.00035	0.02	0.00035	0.0272
a_{max}	0.0037	0.26	0.025	0.37
χ^2_{red}	$7.73272-4$	$2.64754-3$	$5.19042-2$	$4.56595-2$
c_0	-9.05931	-3.96337	-8.88283	$8.93254+3$
b_0	-3.76458	-3.57444	-3.69508	$5.76792+3$
b_1	$6.28593+5$	$1.93427-18$	$3.03135-20$	$5.77029+3$
a_1	1.0	$1.0046-4$	$3.00297-7$	$2.82861-2$
m_1	-14.3443	33.923	28.9189	1.00027
b_2	$\cdots$	$\cdots$	$\cdots$	$3.78160+2$
a_2	$\cdots$	$\cdots$	$\cdots$	$9.39447-2$
m_2	$\cdots$	$\cdots$	$\cdots$	9.04197
b_3	$1.0+24$	$\cdots$	$\cdots$	$\cdots$
a_3	$1.69966-3$	$\cdots$	$\cdots$	$\cdots$
m_3	8.8067	$\cdots$	$\cdots$	$\cdots$
b_4	$\cdots$	$\cdots$	$\cdots$	$\cdots$
a_4	$\cdots$	$\cdots$	$\cdots$	$\cdots$
m_4	$\cdots$	$\cdots$	$\cdots$	$\cdots$

Table 14. Parameters of the analytical approximations to the size distributions for the BARE-AC-FG model.

	PAHs	ACH2	Silicate 1	Silicate 2
A	4.727727$-$7	7.862901$-$12	3.680573$-$7	6.218762$-$13
$a_{\min}$	0.00035	0.02	0.00035	0.026
$a_{\max}$	0.0036	0.28	0.024	0.37
χ^2_{red}	6.30466$-$4	2.69604$-$3	4.25529$-$2	6.01087$-$2
c_0	-8.91244	-3.92513	-8.88283	9.04443$+$3
b_0	-3.72015	-3.54913	-3.69508	5.7679$+$3
b_1	6.78215$+$5	2.13708$-$17	2.17105$-$20	5.77024$+$3
a_1	1.0	2.03908$-$4	3.0$-$7	2.7051$-$2
m_1	-14.2532	34.7835	29.2	1.00024
b_2	$\cdots$	$\cdots$	$\cdots$	3.82848$+$2
a_2	$\cdots$	$\cdots$	$\cdots$	9.39615$-$2
m_2	$\cdots$	$\cdots$	$\cdots$	8.94494
b_3	1.0$+$24	$\cdots$	$\cdots$	$\cdots$
a_3	1.58225$-$3	$\cdots$	$\cdots$	$\cdots$
m_3	8.71891	$\cdots$	$\cdots$	$\cdots$
b_4	$\cdots$	$\cdots$	$\cdots$	$\cdots$
a_4	$\cdots$	$\cdots$	$\cdots$	$\cdots$
m_4	$\cdots$	$\cdots$	$\cdots$	$\cdots$

Table 15.   Parameters of the analytical approximations to the size distributions for the BARE-AC-B model.

	PAHs	ACH2	Silicate 1	Silicate 2
A	$4.47594-7$	$7.813825-12$	$3.157791-7$	$8.130755-13$
$a_{\min}$	0.00035	0.02	0.00035	0.021
$a_{\max}$	0.0037	0.25	0.03	0.33
χ^2_{red}	$8.9447-4$	$1.12192-2$	$9.47682-2$	$2.2829-2$
c_0	-9.1238	-3.79483	-8.95818	$2.38667+4$
b_0	-3.78439	-3.46375	-3.71928	$1.4412+4$
b_1	$6.02165+5$	$3.41188-17$	$4.01642-14$	$1.44139+4$
a_1	1.0	$1.94208-4$	$2.45908-6$	$2.20822-2$
m_1	-14.3958	34.2285	22.8203	1.00016
b_2	$\cdots$	$\cdots$	$\cdots$	$5.12554+2$
a_2	$\cdots$	$\cdots$	$\cdots$	$7.85859-2$
m_2	$\cdots$	$\cdots$	$\cdots$	10.2469
b_3	$1.0+24$	$\cdots$	$\cdots$	$\cdots$
a_3	$1.76358-3$	$\cdots$	$\cdots$	$\cdots$
m_3	8.85147	$\cdots$	$\cdots$	$\cdots$
b_4	$\cdots$	$\cdots$	$\cdots$	$\cdots$
a_4	$\cdots$	$\cdots$	$\cdots$	$\cdots$
m_4	$\cdots$	$\cdots$	$\cdots$	$\cdots$

Table 16.   Parameters of the analytical approximations to the size distributions for the
COMP-AC-S model.

	PAHs	ACH2	Silicate 1	Silicate 2	Composites
A	4.480636−7	2.760470−12	3.758253−7	1.347406−13	2.485468−12
$a_{\min}$	0.00035	0.02	0.00035	0.045	0.02
$a_{\max}$	0.0038	0.25	0.02	0.4	0.91
χ^2_{red}	8.34817−5	1.55806−3	4.91354−4	1.22049−3	1.73353−2
c_0	−9.14864	−3.88834	−8.83908	7.60836+3	−2.61479
b_0	−3.79425	−3.52976	−3.68116	5.77288+3	−2.68416
b_1	9.86507+10	5.2005−24	1.11155−13	2.5083+3	9.97435−31
a_1	1.0	8.805−4	3.68131−5	4.81218−2	2.53994−4
m_1	−14.3335	31.7703	16.6919	1.00005	33.679
b_2	$\cdots$	$\cdots$	$\cdots$	1.27299	$\cdots$
a_2	$\cdots$	$\cdots$	$\cdots$	0.12723	$\cdots$
m_2	$\cdots$	$\cdots$	$\cdots$	6.80997	$\cdots$
b_3	1.0+24	$\cdots$	$\cdots$	$\cdots$	$\cdots$
a_3	1.65191−3	$\cdots$	$\cdots$	$\cdots$	$\cdots$
m_3	8.71635	$\cdots$	$\cdots$	$\cdots$	$\cdots$
b_4	$\cdots$	$\cdots$	$\cdots$	$\cdots$	$\cdots$
a_4	$\cdots$	$\cdots$	$\cdots$	$\cdots$	$\cdots$
m_4	$\cdots$	$\cdots$	$\cdots$	$\cdots$	$\cdots$

Table 17.   Parameters of the analytical approximations to the size distributions for the COMP-AC-FG model.

	PAHs	ACH2	Silicate 1	Silicate 2	Composites
A	4.725913−7	2.868609−12	3.926154−7	1.821520−13	1.320657−12
$a_{\min}$	0.00035	0.02	0.00035	0.036	0.02
$a_{\max}$	0.0035	0.25	0.02	0.4	0.66
χ^2_{red}	1.05143−5	1.93094−3	5.43861−4	6.74454−3	8.39873−4
c_0	−9.38386	−3.91187	−8.82601	1.03553+5	−0.951599
b_0	−3.86273	−3.54546	−3.67646	5.76819+3	−1.81202
b_1	1.37152+13	9.86048−31	3.93265−14	2.50619+3	5.27084−14
a_1	1.0	4.65102−4	3.36955−5	1.13857−18	2.72956−6
m_1	−17.038	38.1558	17.1386	1.00002	12.5346
b_2	$\cdots$	$\cdots$	$\cdots$	1.0829	$\cdots$
a_2	$\cdots$	$\cdots$	$\cdots$	0.120892	$\cdots$
m_2	$\cdots$	$\cdots$	$\cdots$	8.01741	$\cdots$
b_3	1.0+24	$\cdots$	$\cdots$	$\cdots$	1.00014+3
a_3	1.60933−3	$\cdots$	$\cdots$	$\cdots$	0.298067
m_3	8.66626	$\cdots$	$\cdots$	$\cdots$	5.93761
b_4	$\cdots$	$\cdots$	$\cdots$	$\cdots$	$\cdots$
a_4	$\cdots$	$\cdots$	$\cdots$	$\cdots$	$\cdots$
m_4	$\cdots$	$\cdots$	$\cdots$	$\cdots$	$\cdots$

Table 18.   Parameters of the analytical approximations to the size distributions for the COMP-AC-B model.

	PAHs	ACH2	Silicate 1	Silicate 2	Composites
A	4.470182−7	2.068952−13	3.383484−7	7.022871−14	4.516269−12
$a_{\min}$	0.00035	0.022	0.00035	0.046	0.02
$a_{\max}$	0.0039	0.21	0.02	0.25	0.7
χ^2_{red}	1.36914−5	3.5196−5	4.2771−4	2.93878−5	2.0045−3
c_0	−9.6296	−3.92565	−8.82349	−6.03894	−2.70635
b_0	−3.94002	−4.49943	−3.67603	−7.42085	−2.66966
b_1	1.37152+13	0.64013	8.30679−29	10.7406	1.60242−19
a_1	1.0	6.90874−2	6.23404−7	0.106099	2.60559−4
m_1	−17.2214	9.27863	28.0109	9.89337	21.4322
b_2	$\cdots$	0.94057	$\cdots$	0.698926	$\cdots$
a_2	$\cdots$	0.115074	$\cdots$	0.231661	$\cdots$
m_2	$\cdots$	1.85136	$\cdots$	3.02112	$\cdots$
b_3	1.0+24	$\cdots$	$\cdots$	$\cdots$	$\cdots$
a_3	1.81574−3	$\cdots$	$\cdots$	$\cdots$	$\cdots$
m_3	8.82131	$\cdots$	$\cdots$	$\cdots$	$\cdots$
b_4	$\cdots$	$\cdots$	$\cdots$	$\cdots$	$\cdots$
a_4	$\cdots$	$\cdots$	$\cdots$	$\cdots$	$\cdots$
m_4	$\cdots$	$\cdots$	$\cdots$	$\cdots$	$\cdots$

Table 19.   Parameters of the analytical approximations to the size distributions for the COMP-NC-S model.

	PAHs	Silicate 1	Silicate 2	Composites
A	$4.457245-7$	$3.894306-7$	$8.424593-14$	$3.936063-12$
$a_{\min}$	0.00035	0.00035	0.048	0.02
$a_{\max}$	0.0036	0.02	0.34	0.8
χ^2_{red}	$9.09294-6$	$5.38936-4$	$1.45554-3$	$3.85852-3$
c_0	-9.36312	-8.82792	$7.40265+3$	-2.48599
b_0	-3.85681	-3.67806	$5.76918+3$	-2.58455
b_1	$2.68843+12$	$2.89768-20$	$2.50652+3$	$9.87203-31$
a_1	1.0	$7.88794-6$	$5.21321-2$	$6.35373-6$
m_1	-16.1999	22.3415	1.0003	28.5023
b_2	$\cdots$	$\cdots$	2.32676	$\cdots$
a_2	$\cdots$	$\cdots$	0.127735	$\cdots$
m_2	$\cdots$	$\cdots$	7.0254	$\cdots$
b_3	$1.0+24$	$\cdots$	$\cdots$	$\cdots$
a_3	$1.68273-3$	$\cdots$	$\cdots$	$\cdots$
m_3	8.74084	$\cdots$	$\cdots$	$\cdots$
b_4	$\cdots$	$\cdots$	$\cdots$	$\cdots$
a_4	$\cdots$	$\cdots$	$\cdots$	$\cdots$
m_4	$\cdots$	$\cdots$	$\cdots$	$\cdots$

Table 20.   Parameters of the analytical approximations to the size distributions for the COMP-NC-FG model.

	PAHs	Silicate 1	Silicate 2	Composites
A	4.703264−7	4.093516−7	8.907133−14	2.552983−12
$a_{\min}$	0.00035	0.00035	0.0489	0.019
$a_{\max}$	0.0035	0.02	0.36	0.85
χ^2_{red}	7.51744−6	8.68976−4	8.60985−3	3.52374−3
c_0	−9.23696	−8.78955	7.40319+3	−1.64917
b_0	−3.81837	−3.66574	5.76731+3	−2.01144
b_1	2.68843+12	9.91223−31	2.50684+3	1.7781−28
a_1	1.0	7.68829−7	5.20919−2	3.42324−7
m_1	−16.0932	30.2697	0.999787	24.2268
b_2	$\cdots$	$\cdots$	2.95527	$\cdots$
a_2	$\cdots$	$\cdots$	0.12907	$\cdots$
m_2	$\cdots$	$\cdots$	5.4247	$\cdots$
b_3	1.0+24	$\cdots$	$\cdots$	$\cdots$
a_3	1.55501−3	$\cdots$	$\cdots$	$\cdots$
m_3	8.62883	$\cdots$	$\cdots$	$\cdots$
b_4	$\cdots$	$\cdots$	$\cdots$	$\cdots$
a_4	$\cdots$	$\cdots$	$\cdots$	$\cdots$
m_4	$\cdots$	$\cdots$	$\cdots$	$\cdots$

Table 21. Parameters of the analytical approximations to the size distributions for the COMP-NC-B model.

	PAHs	Silicate 1	Silicate 2	Composites
A	$4.473155-7$	$3.368198-7$	$3.037852-14$	$5.103841-12$
a_{min}	0.00035	0.00035	0.0579	0.02
a_{max}	0.0038	0.02	0.18	0.8
χ^2_{red}	$1.14807-5$	$6.28528-4$	$3.43037-5$	$9.61637-3$
c_0	-9.45486	-8.81100	$7.03663+3$	-2.86045
b_0	-3.8855	-3.67229	$5.77097+3$	-2.84458
b_1	$2.68843+12$	$9.83854-31$	$2.50716+3$	$9.97738-31$
a_1	1.0	$4.07425-7$	$6.0368-2$	$2.03298-4$
m_1	-16.2777	29.4547	1.00102	33.5112
b_2	$\cdots$	$\cdots$	26.3599	$\cdots$
a_2	$\cdots$	$\cdots$	$9.2944-2$	$\cdots$
m_2	$\cdots$	$\cdots$	5.99341	$\cdots$
b_3	$1.0+24$	$\cdots$	$\cdots$	$\cdots$
a_3	$1.7925-3$	$\cdots$	$\cdots$	$\cdots$
m_3	8.82824	$\cdots$	$\cdots$	$\cdots$
b_4	$\cdots$	$\cdots$	$\cdots$	$\cdots$
a_4	$\cdots$	$\cdots$	$\cdots$	$\cdots$
m_4	$\cdots$	$\cdots$	$\cdots$	$\cdots$
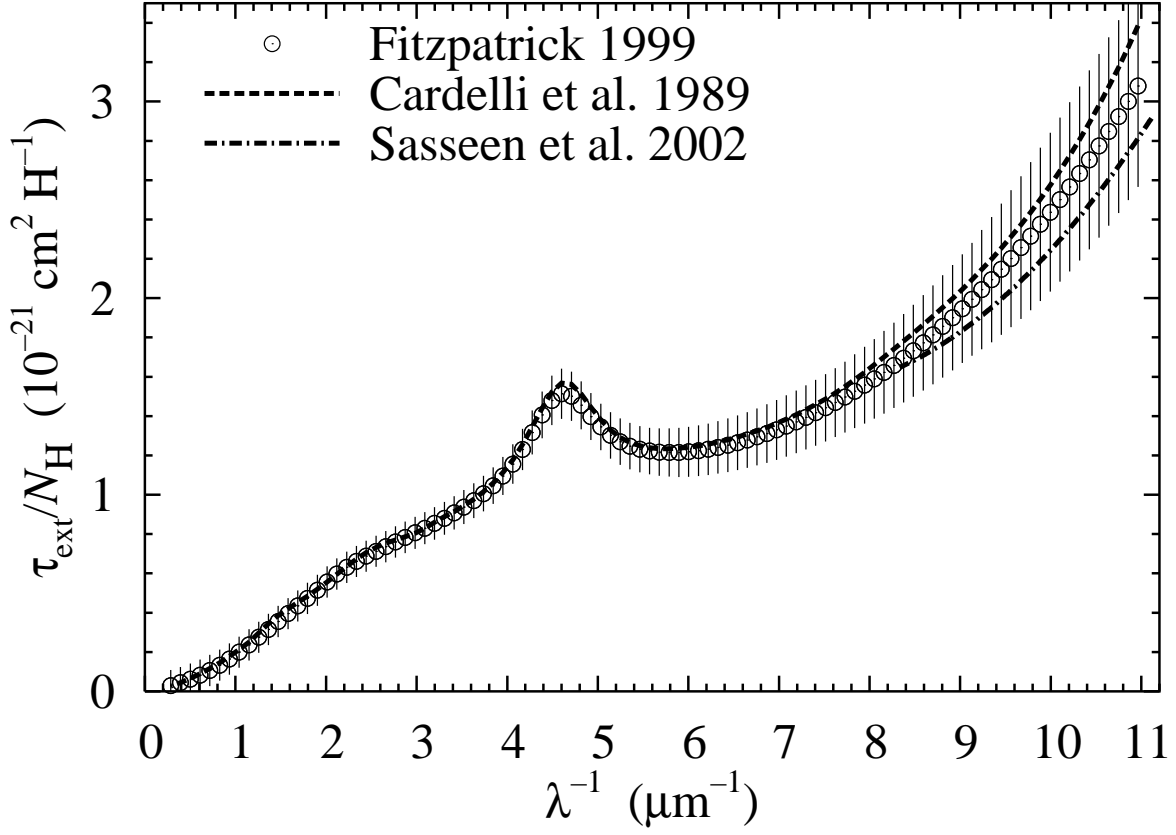
Fig. 1.— The mean extinction curve of the diffuse interstellar medium with R_V=3.1 from Fitzpatrick (1999) together with the curve from Cardelli et al. (1989) and the new FUV curve from Sasseen et al. (2002)
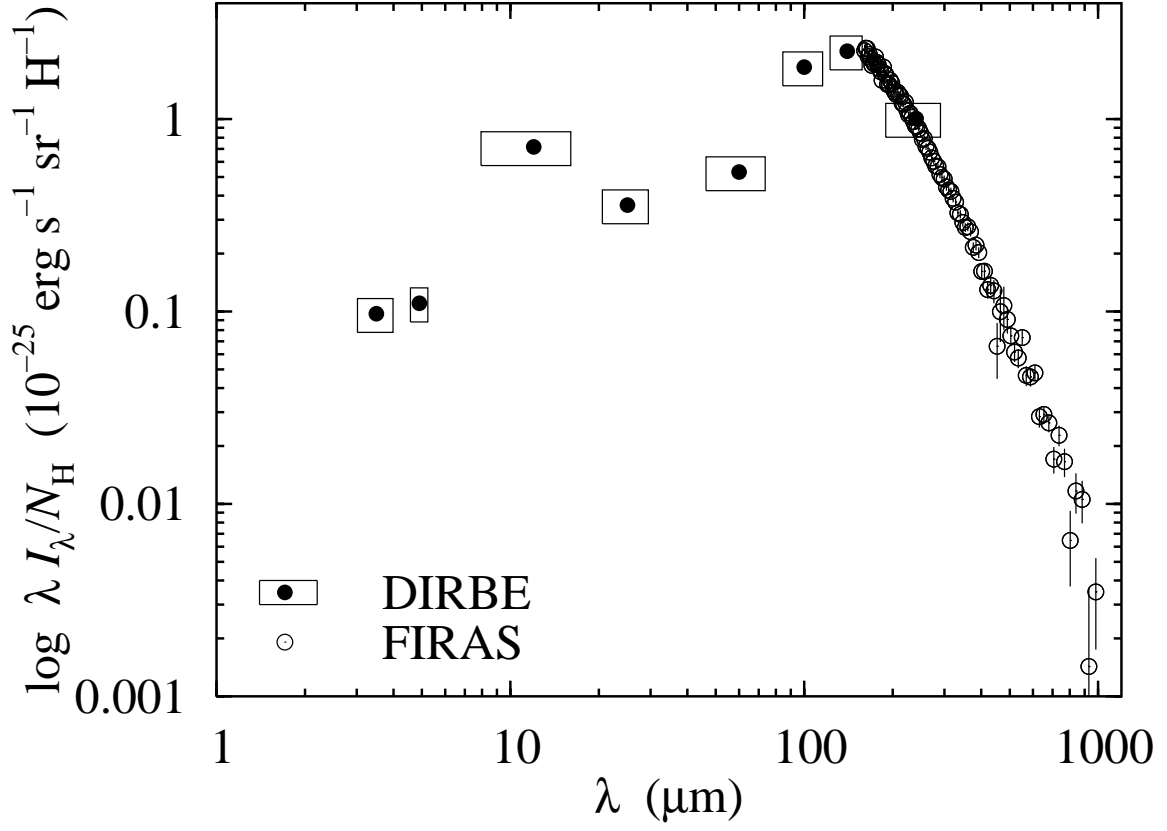
Fig. 2.— Specific intensity per hydrogen atom of dust emission at high Galactic latitudes, $|b| \geq 25°$. Observational data are from DIRBE (Arendt et al. 1998) and FIRAS (Dwek et al. 1997)
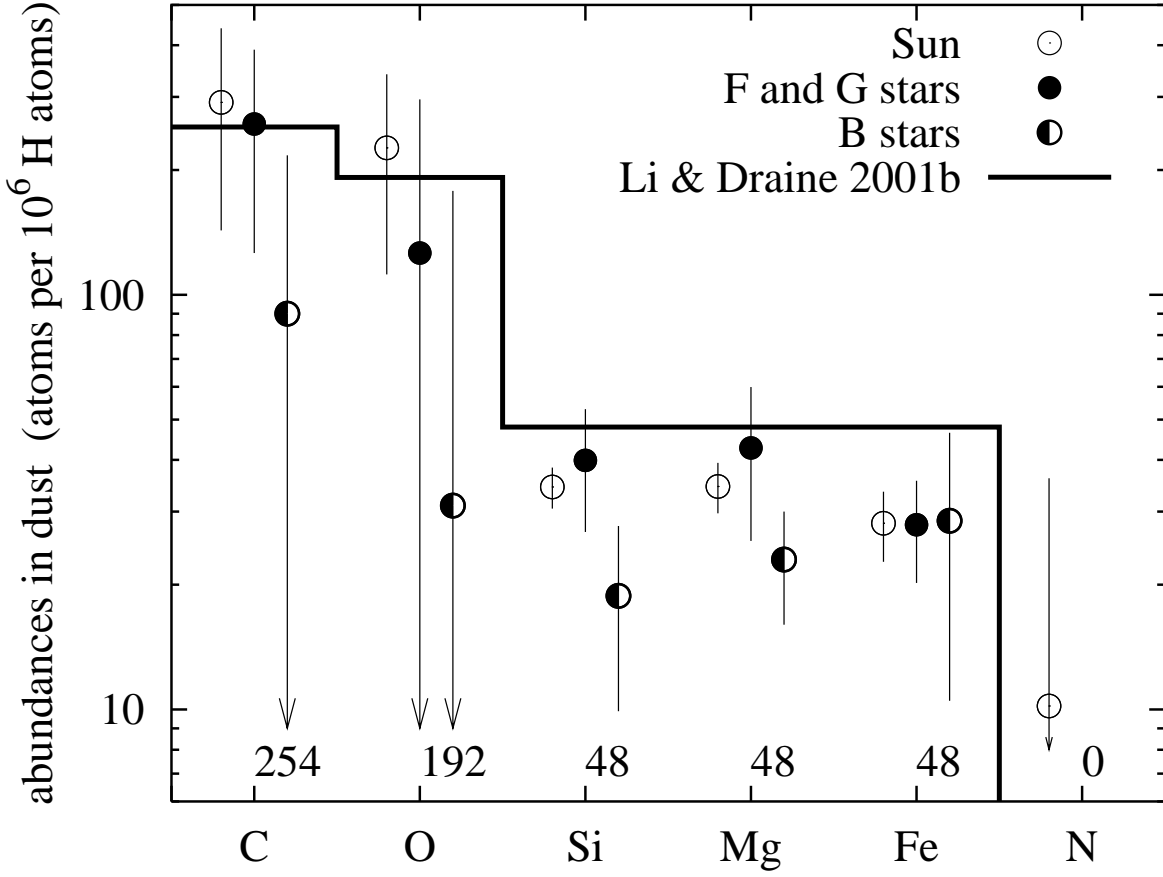
Fig. 3.— The elemental abundances in dust derived by assuming the interstellar abundances to be solar those for F and G stars, and B stars. Numbers along the abscissa are the Li & Draine (2001b) abundances.
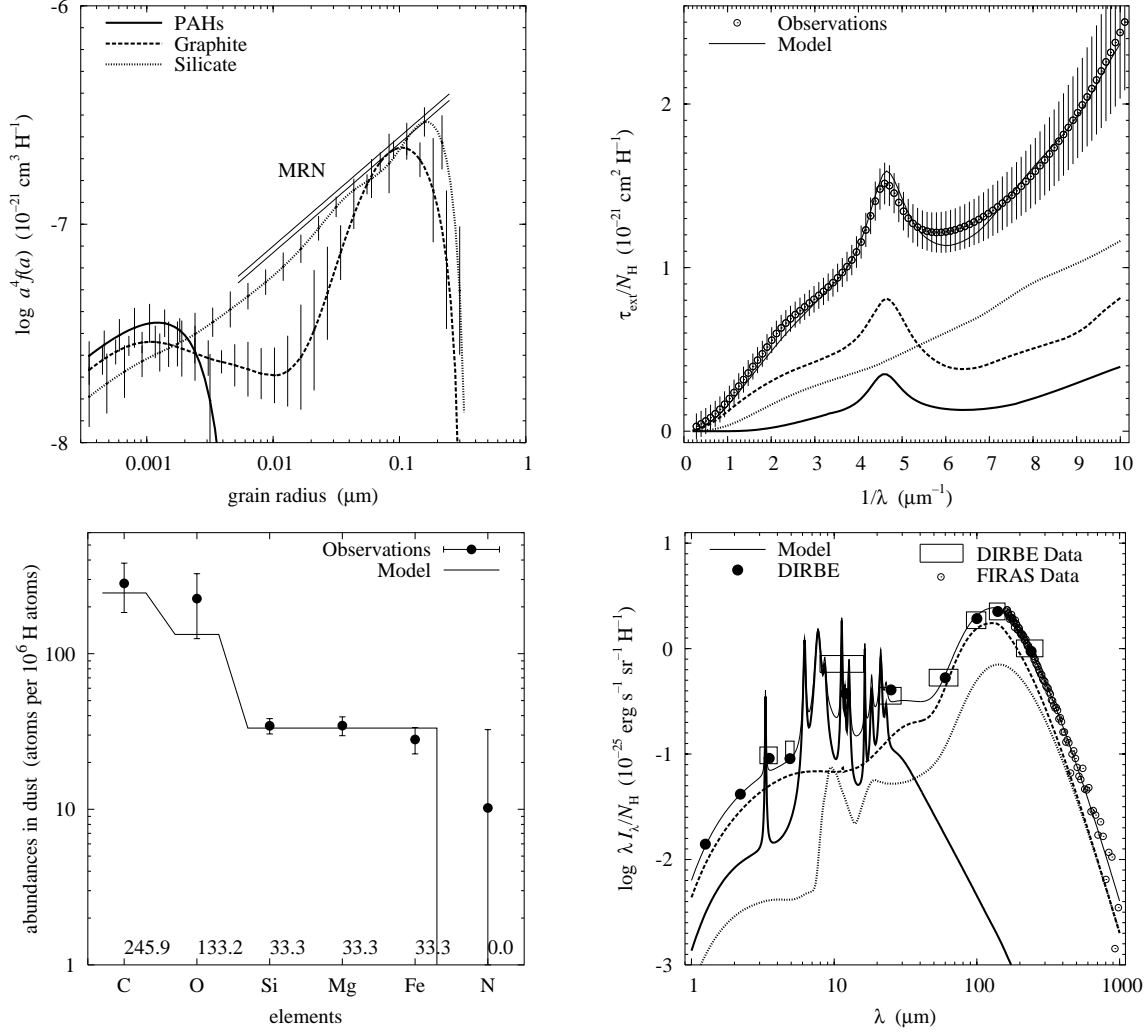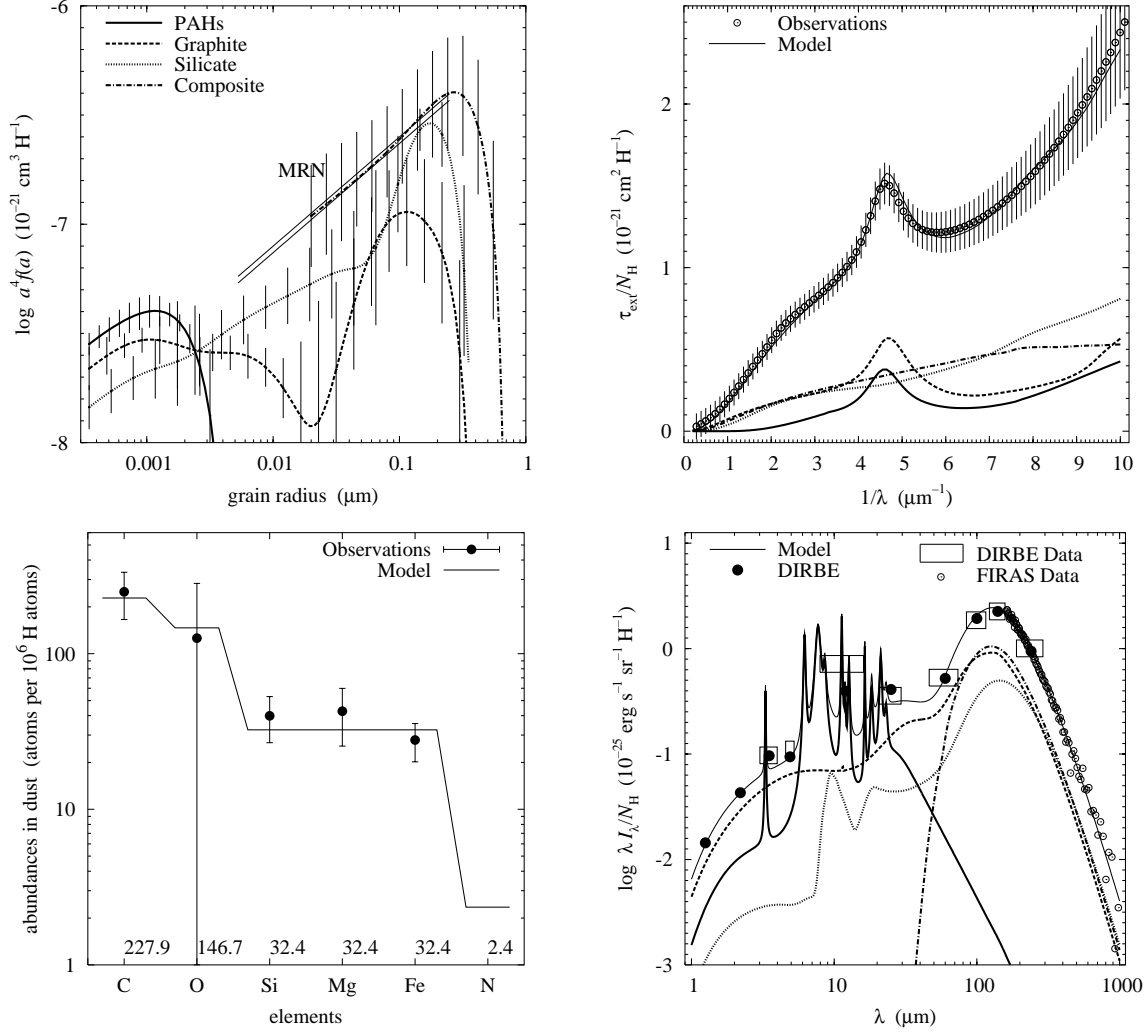
Fig. 4.— BARE-GR-S dust model: the size distributions (top left), extinction curve (top right), elemental requirements (bottom left), and emission spectrum (bottom right). Two straight lines are the MRN size distributions for silicate (upper line) and graphite (lower line).
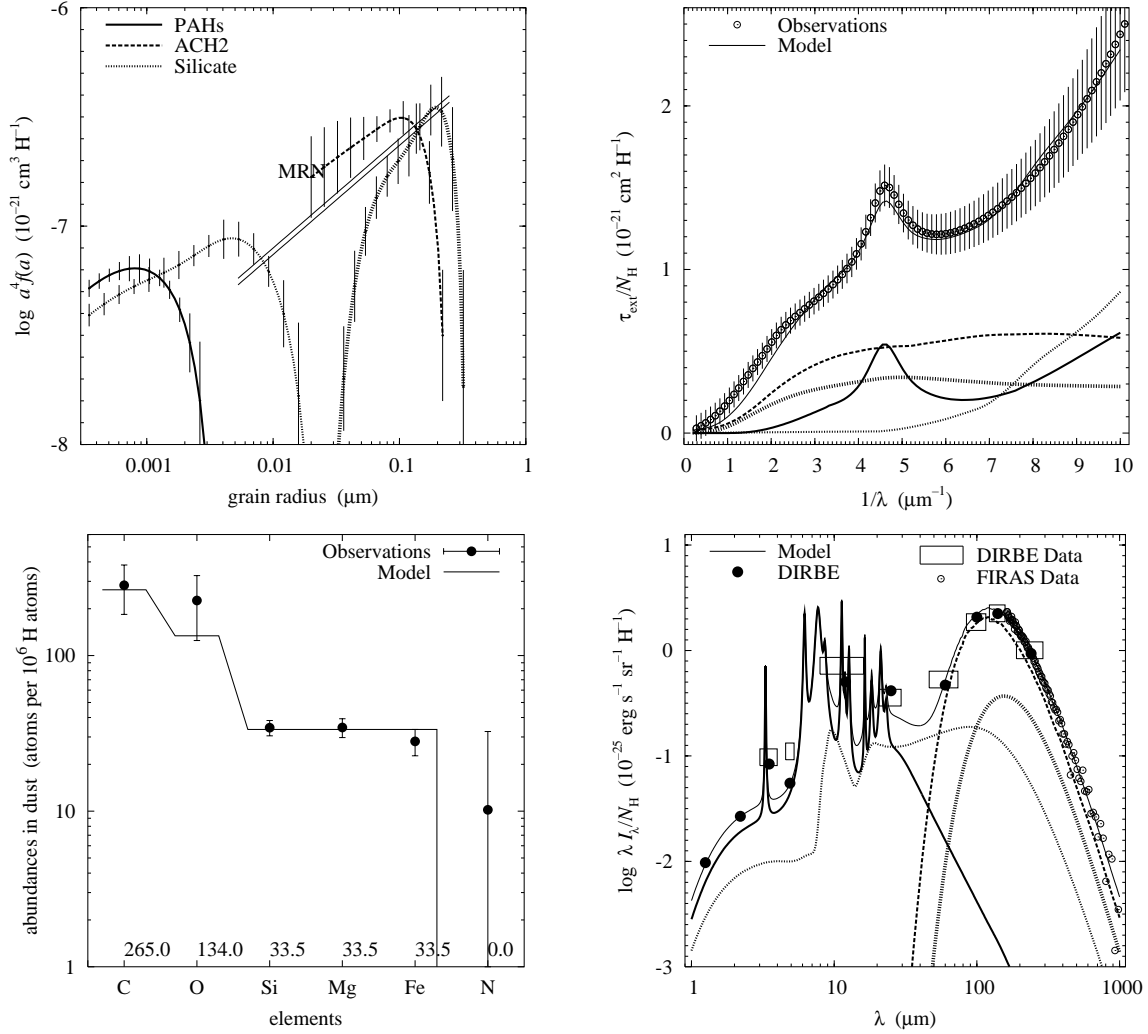
Fig. 5.— BARE-AC-S dust model: the size distributions (top left), extinction curve (top right), elemental requirements (bottom left), and emission spectrum (bottom right). Various populations of the same dust component are depicted by the lines of various width. Two straight lines are the MRN size distributions for silicate (upper line) and graphite (lower line).
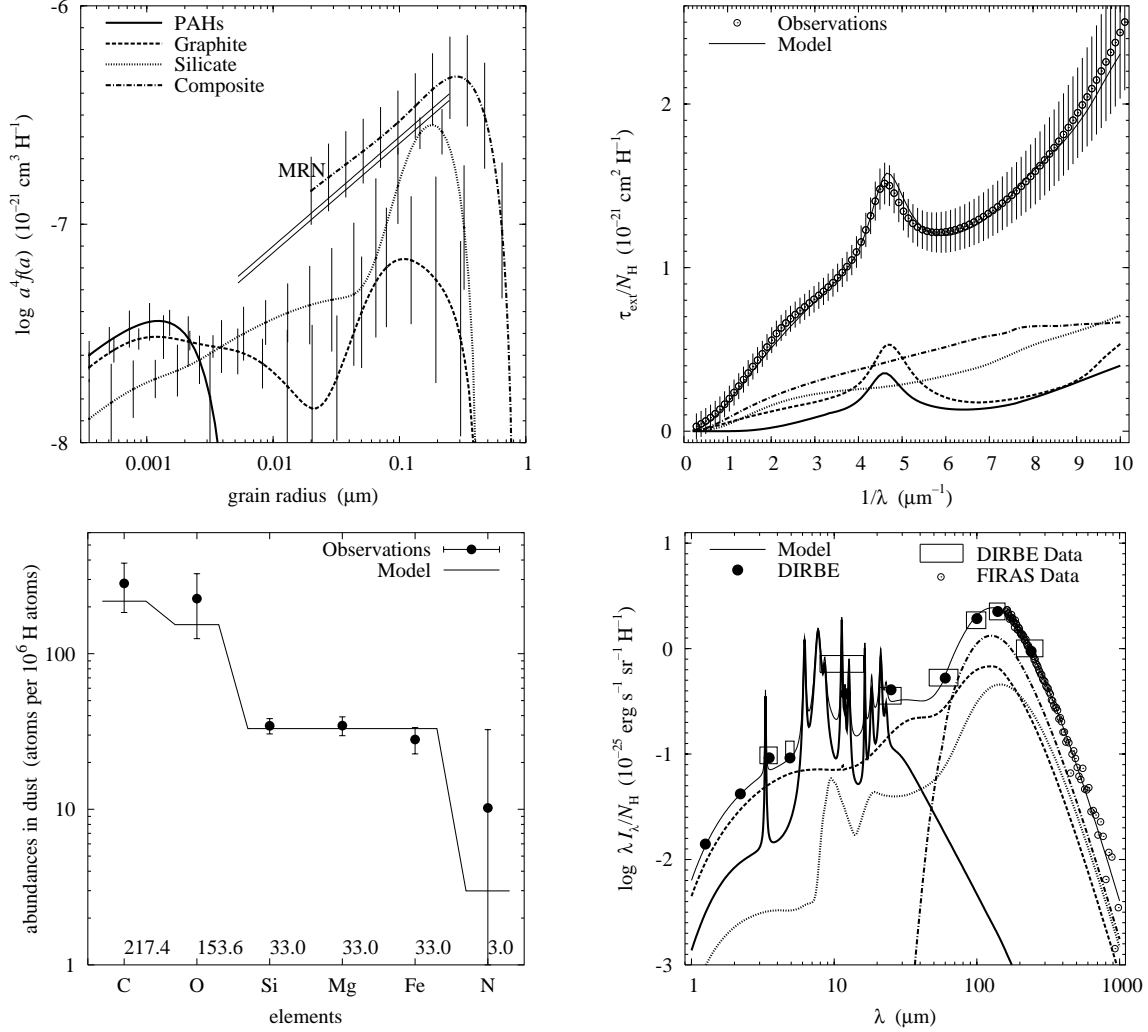
Fig. 6.— COMP-GR-S dust model: the size distributions (top left), extinction curve (top right), elemental requirements (bottom left), and emission spectrum (bottom right). Two straight lines are the MRN size distributions for silicate (upper line) and graphite (lower line).
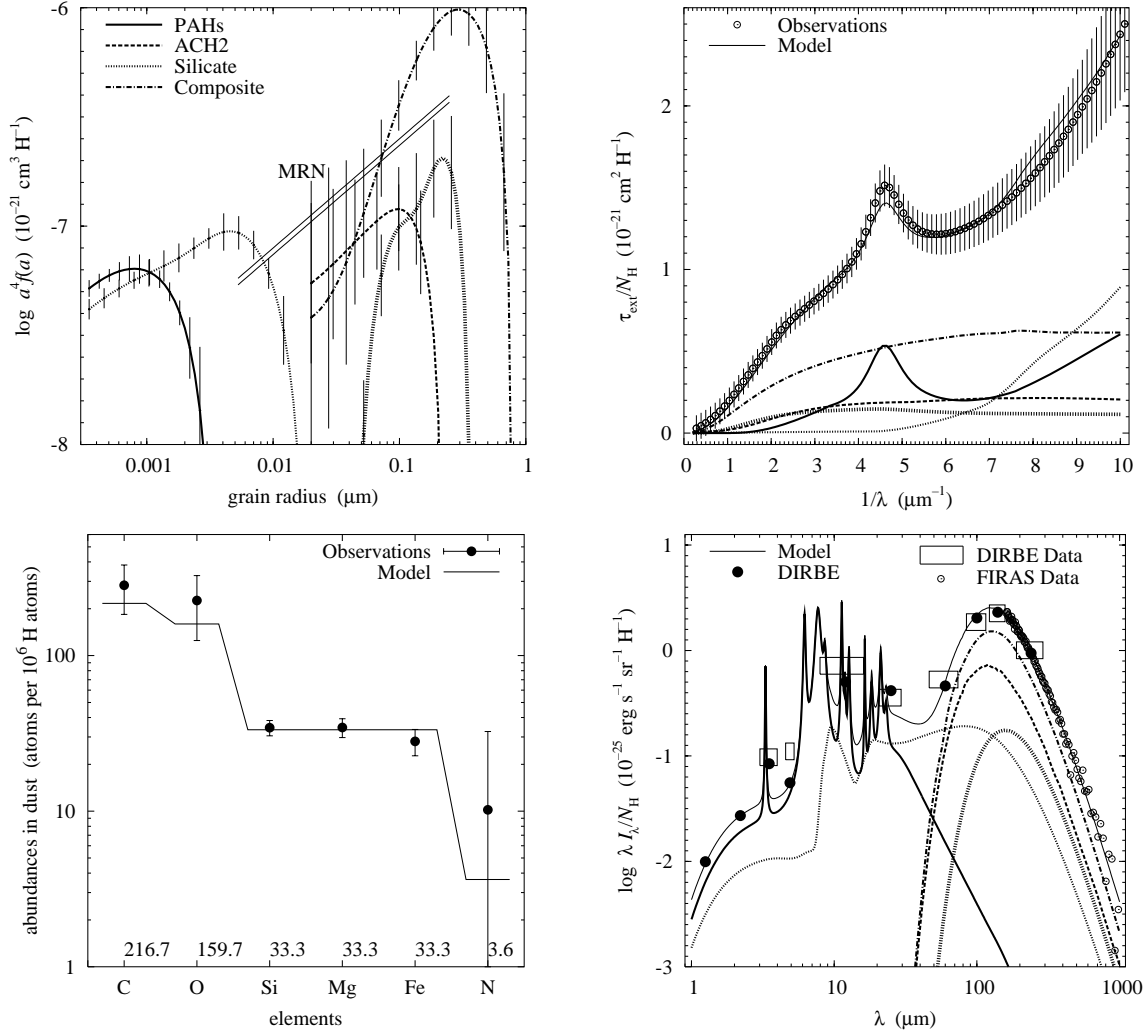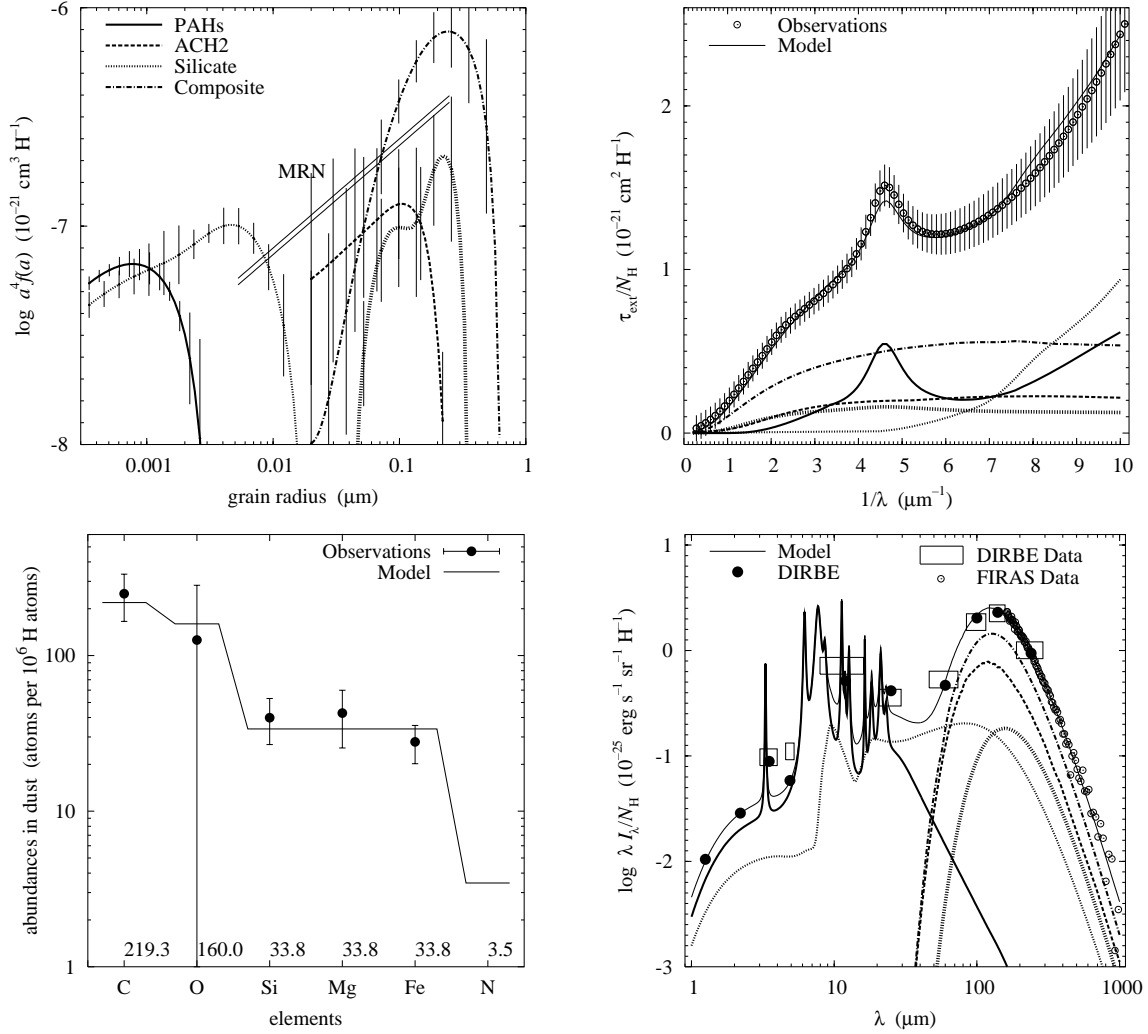
Fig. 7.— COMP-AC-S dust model: the size distributions (top left), extinction curve (top right), elemental requirements (bottom left), and emission spectrum (bottom right). Various populations of the same dust component are depicted by the lines of various width. Two straight lines are the MRN size distributions for silicate (upper line) and graphite (lower line).
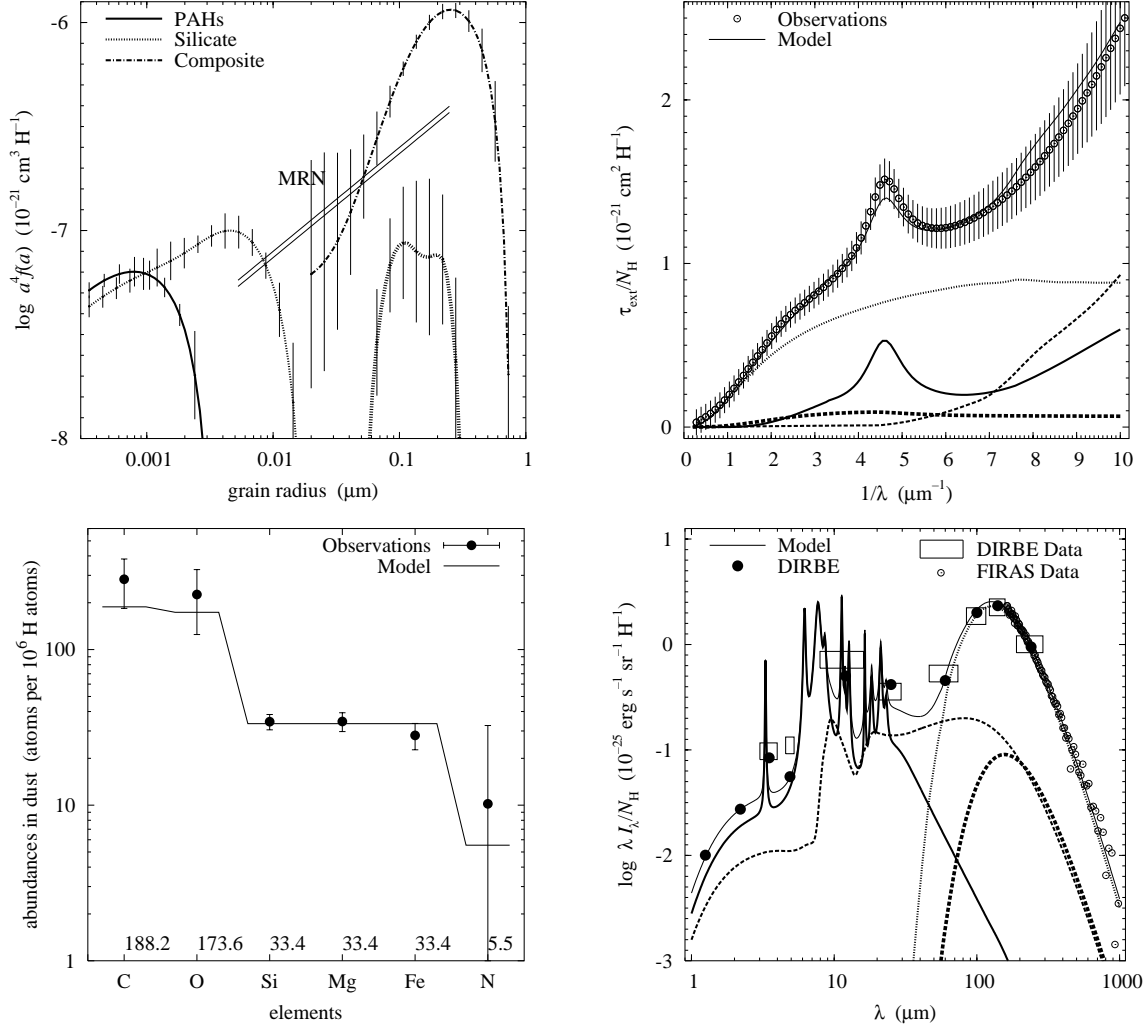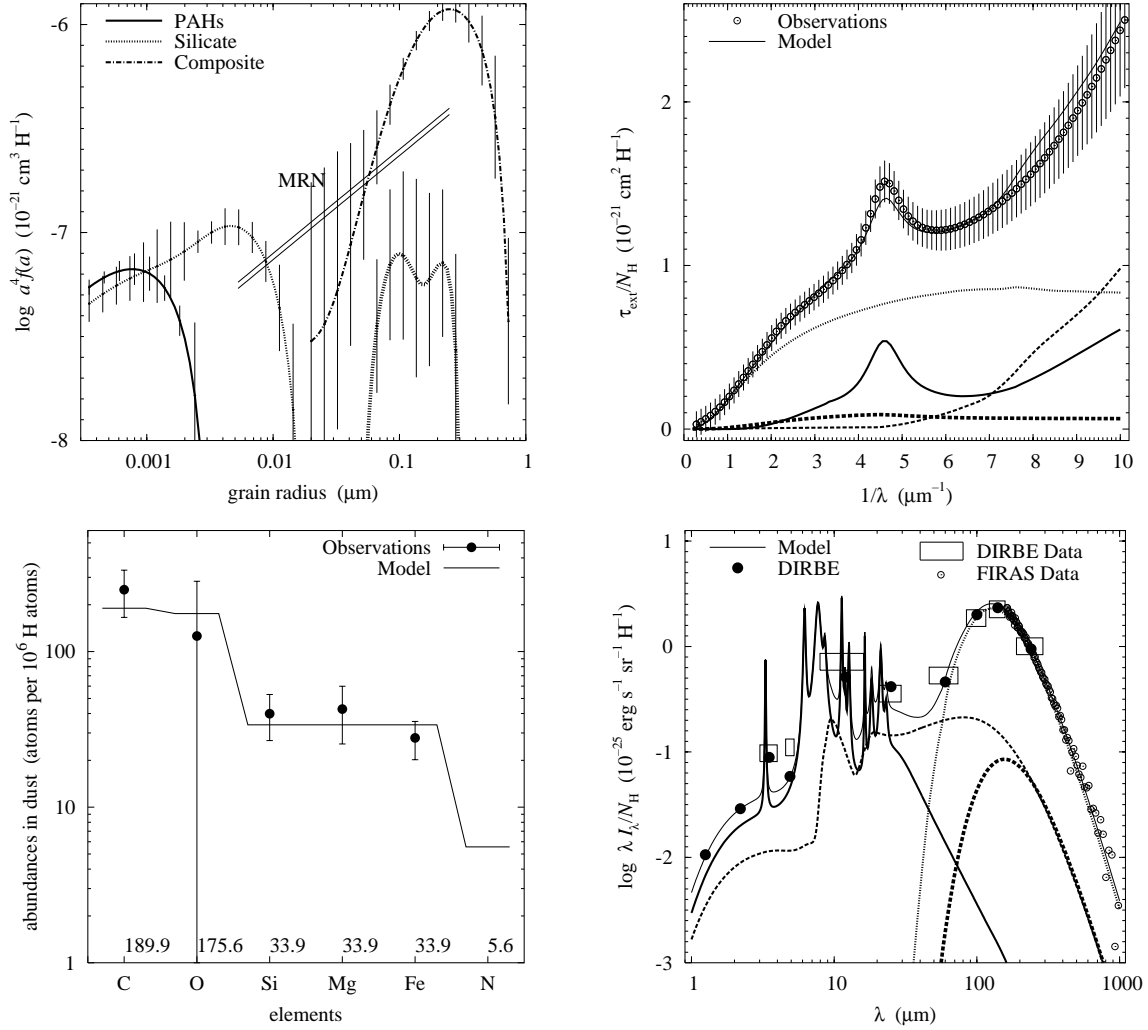
Fig. 8.— COMP-NC-S dust model: the size distributions (top left), extinction curve (top right), elemental requirements (bottom left), and emission spectrum (bottom right). Various populations of the same dust component are depicted by the lines of various width. Two straight lines are the MRN size distributions for silicate (upper line) and graphite (lower line).
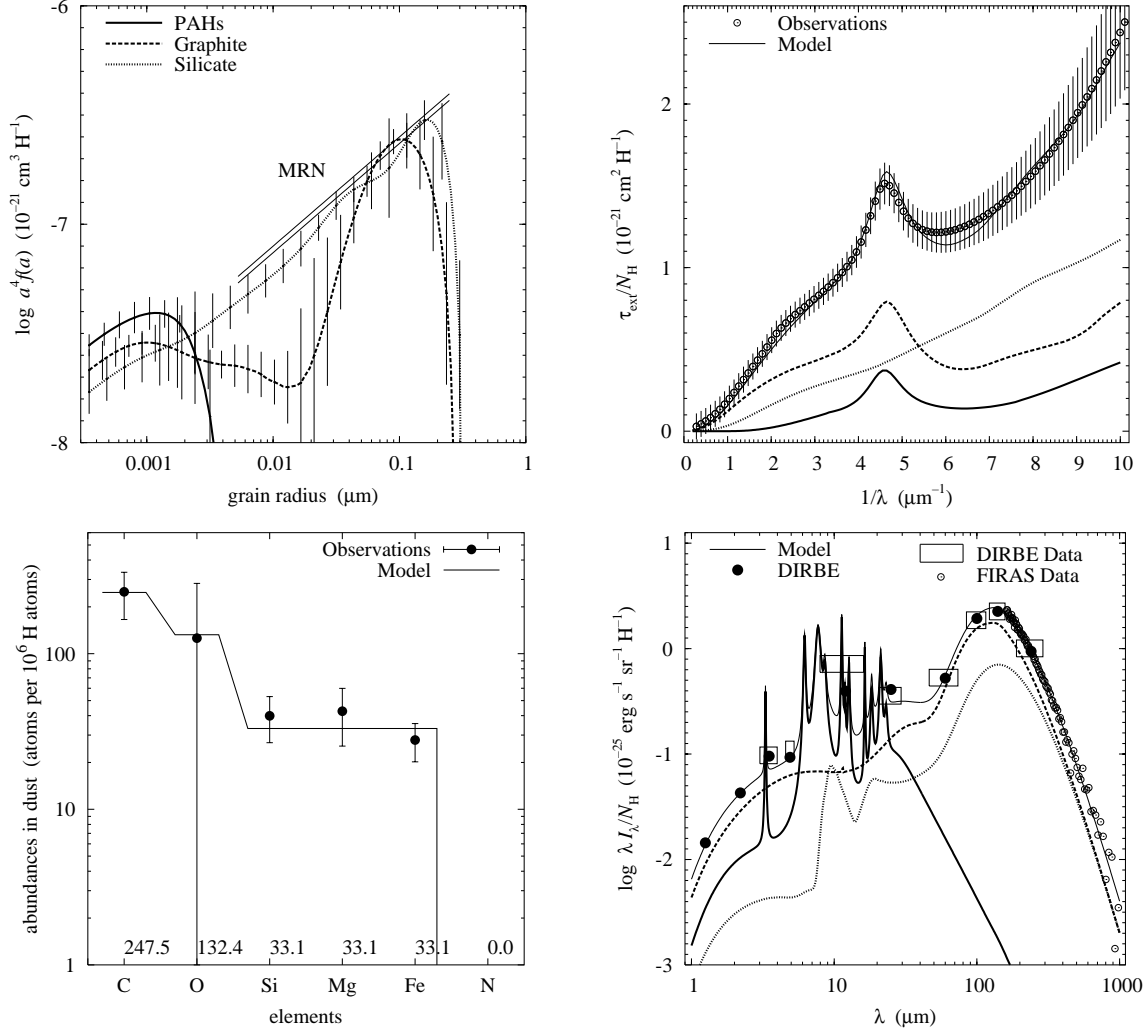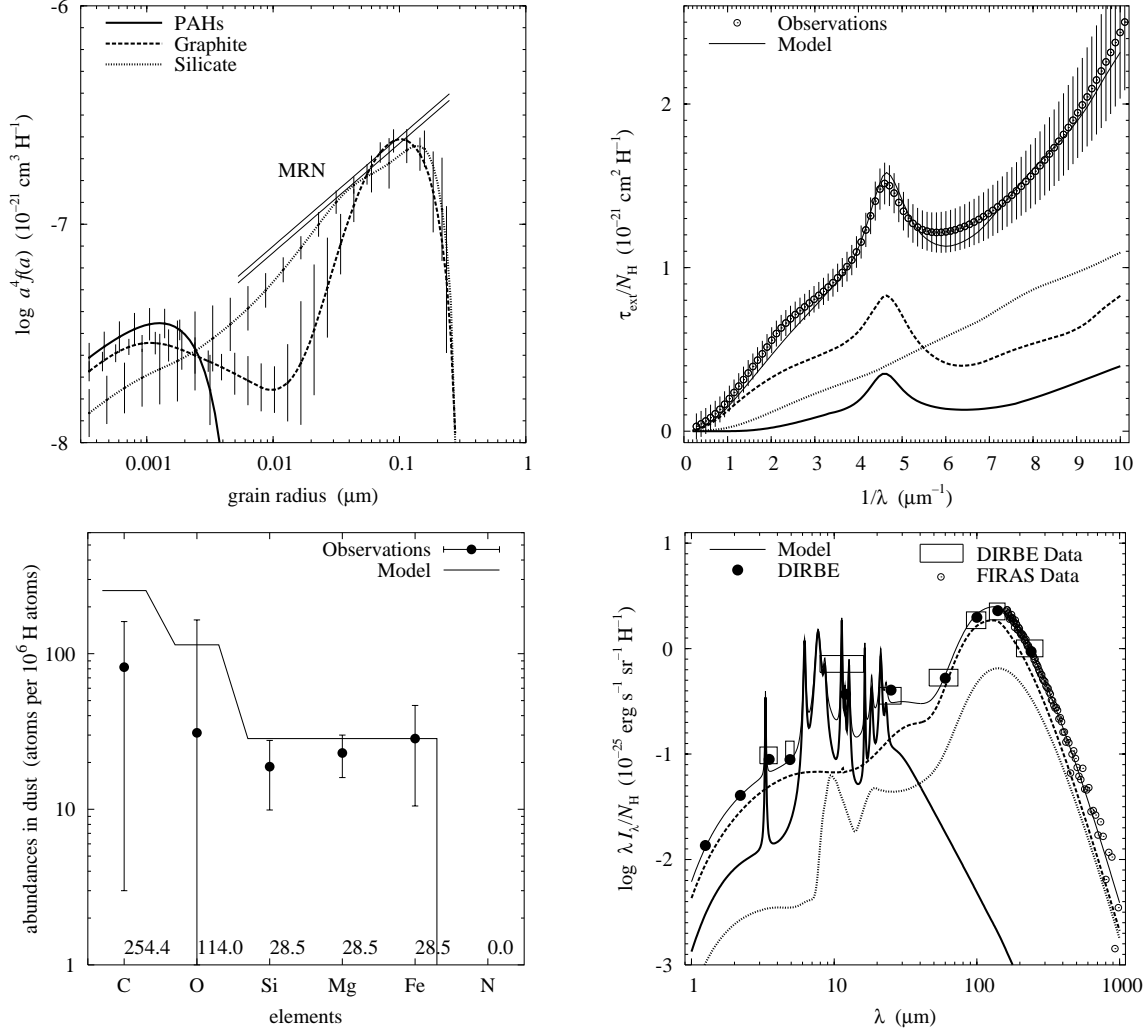
Fig. 9.— BARE-GR-FG dust model: the size distributions (top left), extinction curve (top right), elemental requirements (bottom left), and emission spectrum (bottom right). Two straight lines are the MRN size distributions for silicate (upper line) and graphite (lower line).
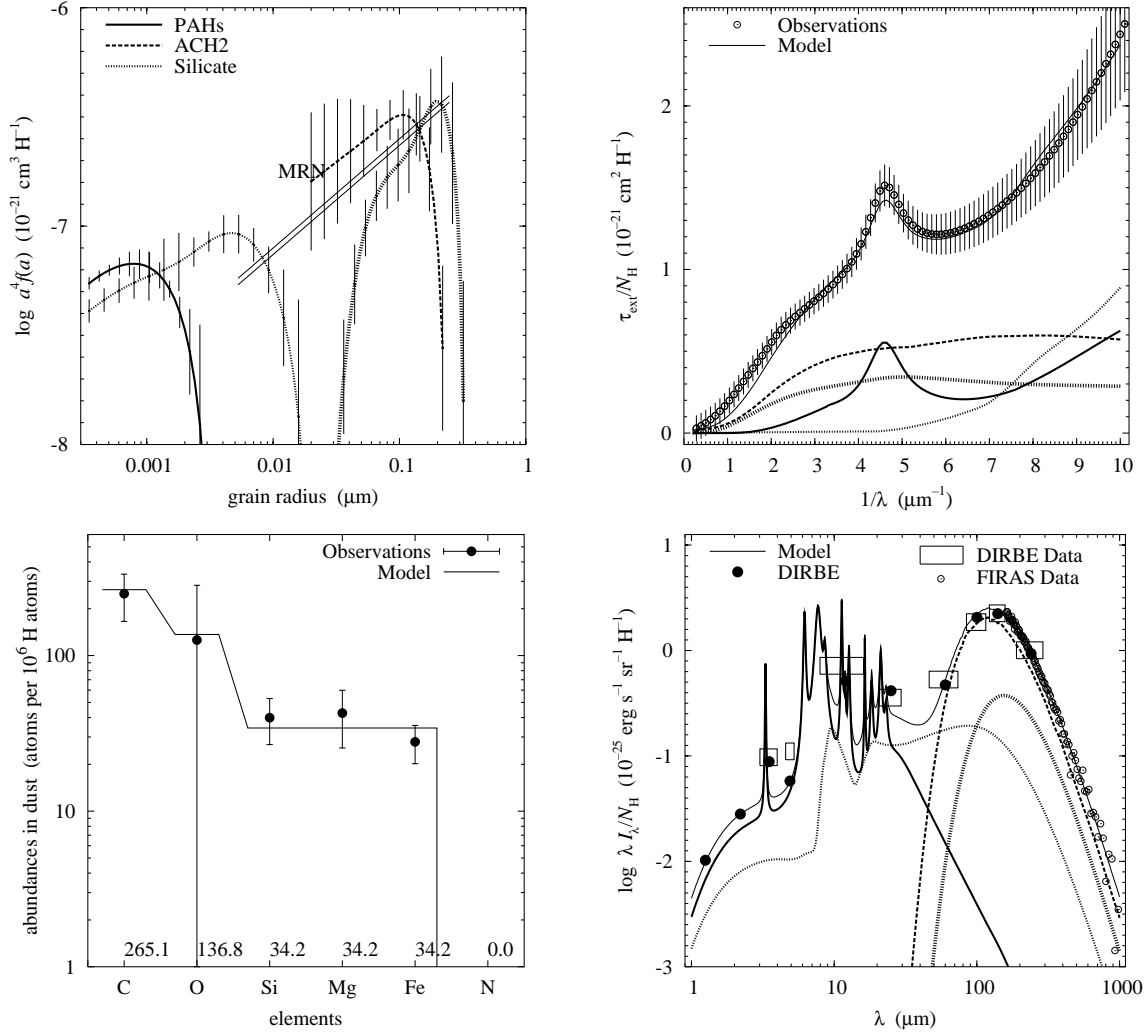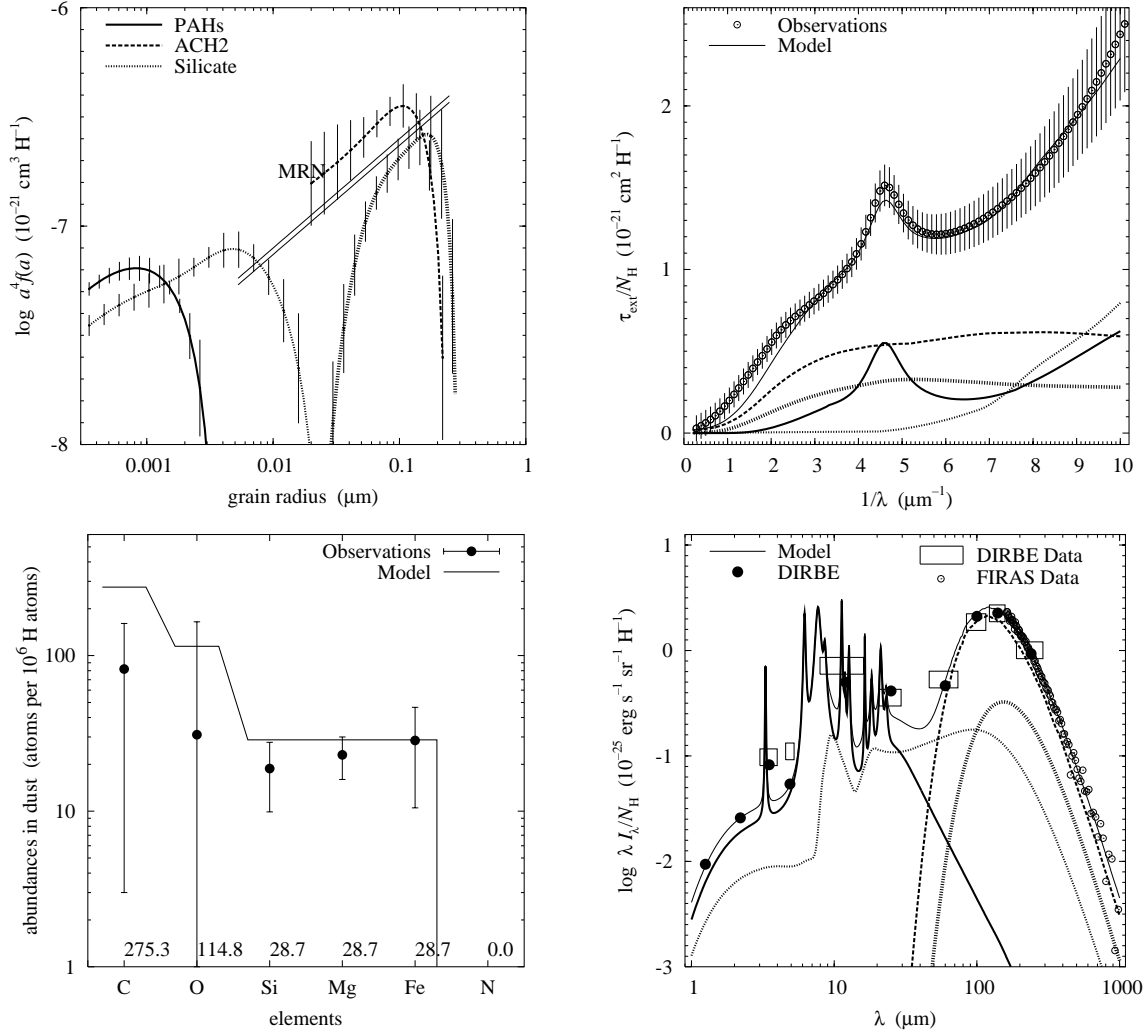
Fig. 10.— BARE-AC-FG dust model: the size distributions (top left), extinction curve (top right), elemental requirements (bottom left), and emission spectrum (bottom right). Various populations of the same dust component are depicted by the lines of various width. Two straight lines are the MRN size distributions for silicate (upper line) and graphite (lower line).

Fig. 11.— COMP-GR-FG dust model: the size distributions (top left), extinction curve (top right), elemental requirements (bottom left), and emission spectrum (bottom right). Two straight lines are the MRN size distributions for silicate (upper line) and graphite (lower line).

Fig. 12.— COMP-AC-FG dust model: the size distributions (top left), extinction curve (top right), elemental requirements (bottom left), and emission spectrum (bottom right). Various populations of the same dust component are depicted by the lines of various width. Two straight lines are the MRN size distributions for silicate (upper line) and graphite (lower line).
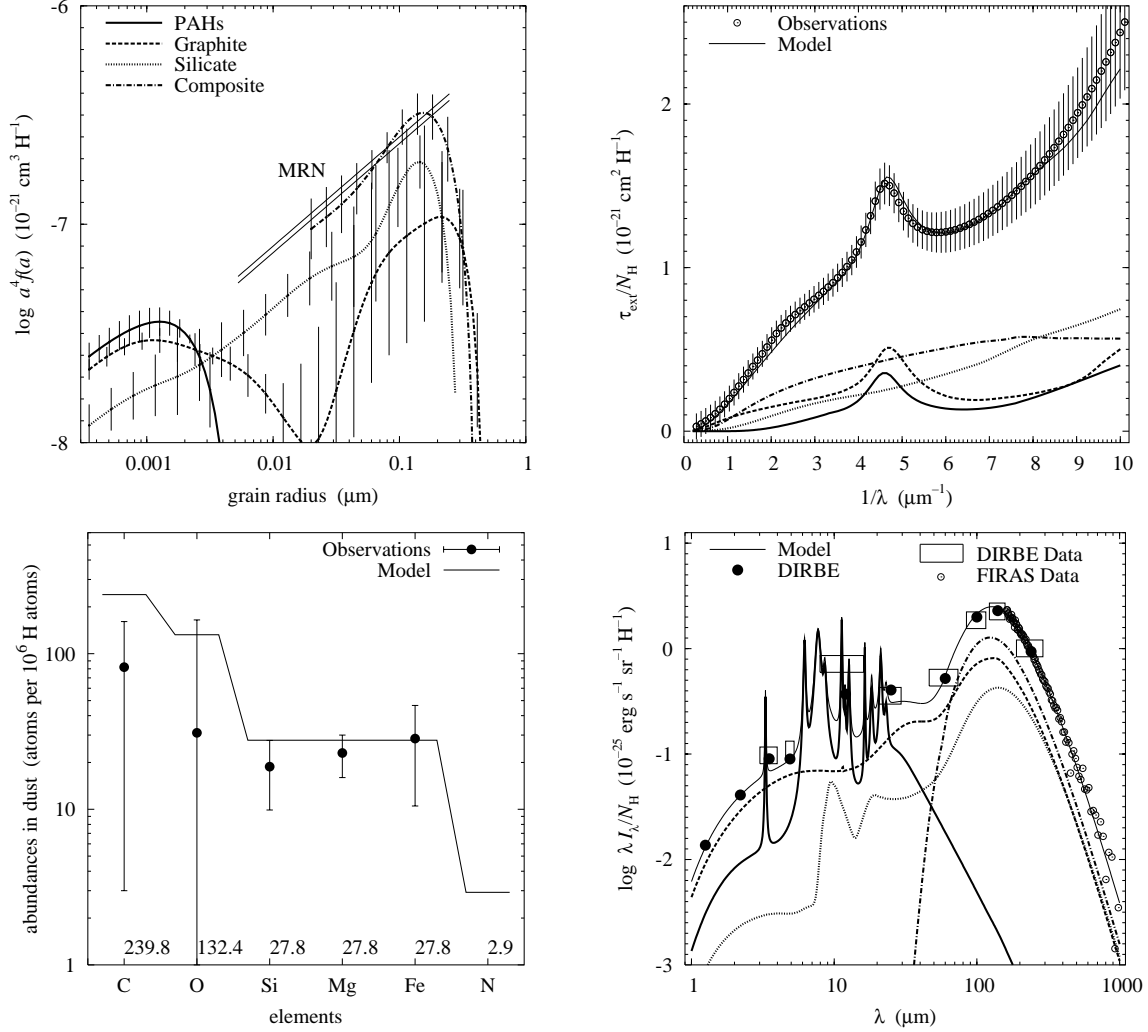
Fig. 13.— COMP-NC-FG dust model: the size distributions (top left), extinction curve (top right), elemental requirements (bottom left), and emission spectrum (bottom right). Various populations of the same dust component are depicted by the lines of various width. Two straight lines are the MRN size distributions for silicate (upper line) and graphite (lower line).

Fig. 14.— BARE-GR-B dust model: the size distributions (top left), extinction curve (top right), elemental requirements (bottom left), and emission spectrum (bottom right). Two straight lines are the MRN size distributions for silicate (upper line) and graphite (lower line).
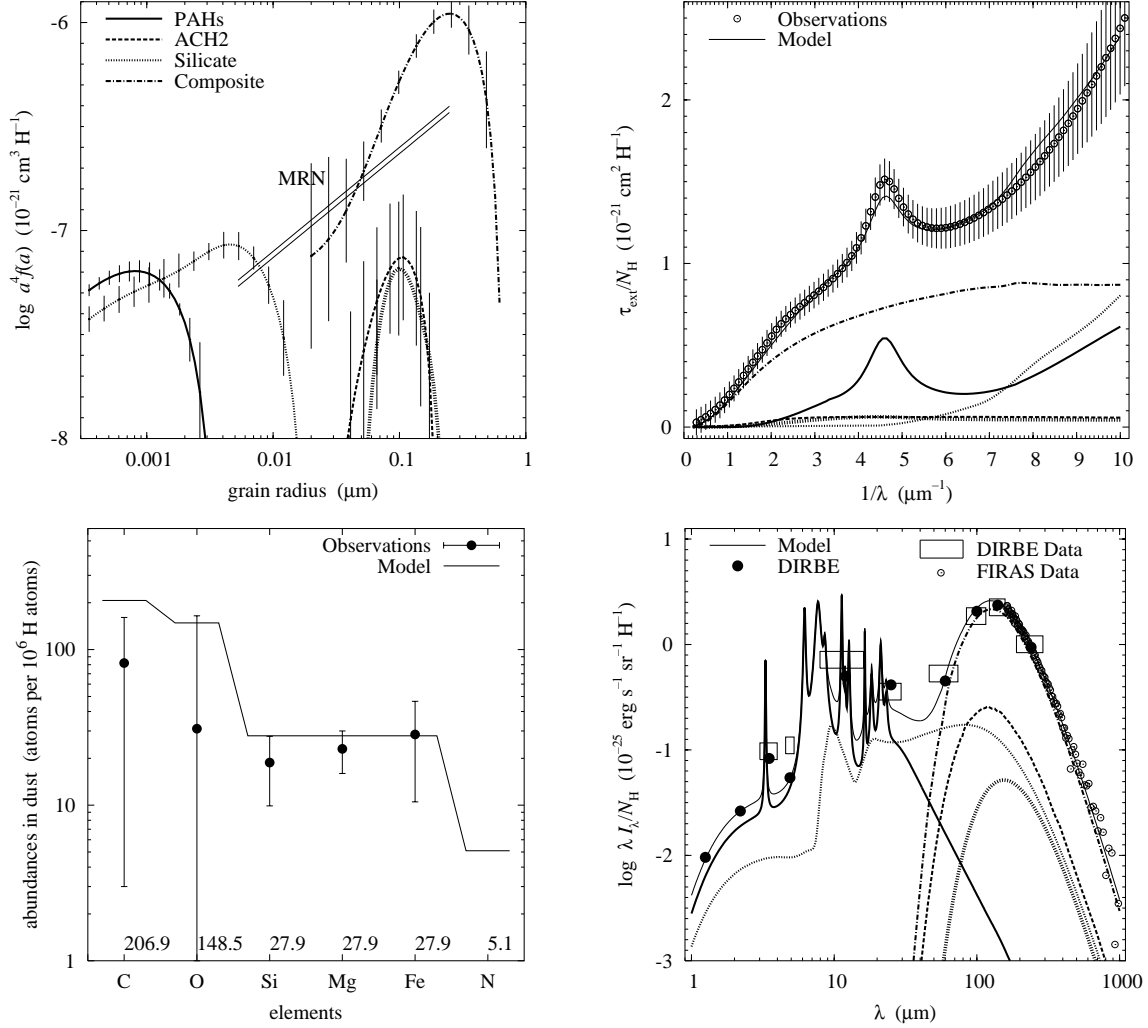
Fig. 15.— BARE-AC-B dust model: the size distributions (top left), extinction curve (top right), elemental requirements (bottom left), and emission spectrum (bottom right). Various populations of the same dust component are depicted by the lines of various width. Two straight lines are the MRN size distributions for silicate (upper line) and graphite (lower line).
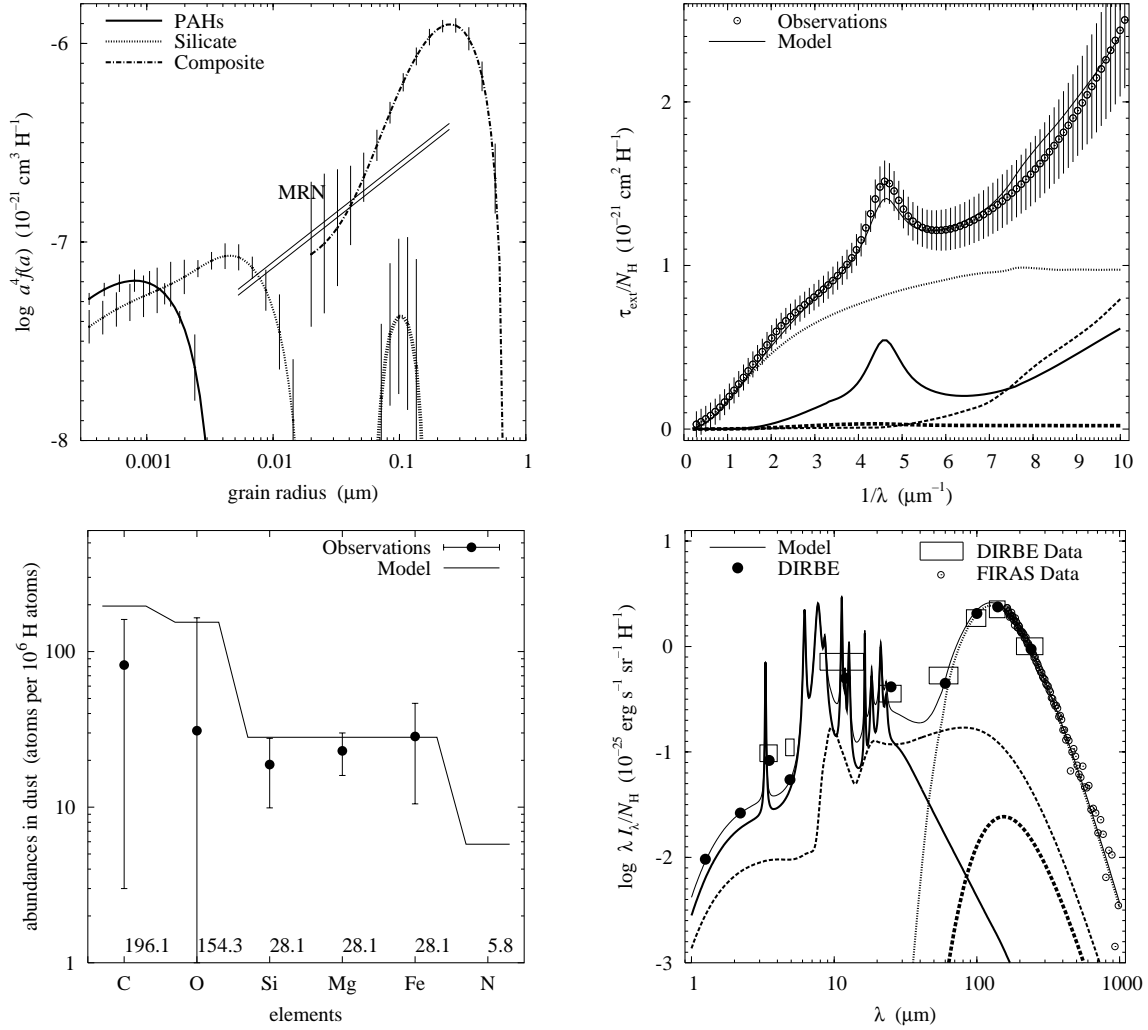
Fig. 16.— COMP-GR-B dust model: the size distributions (top left), extinction curve (top right), elemental requirements (bottom left), and emission spectrum (bottom right). Two straight lines are the MRN size distributions for silicate (upper line) and graphite (lower line).

Fig. 17.— COMP-AC-B dust model: the size distributions (top left), extinction curve (top right), elemental requirements (bottom left), and emission spectrum (bottom right). Various populations of the same dust component are depicted by the lines of various width. Two straight lines are the MRN size distributions for silicate (upper line) and graphite (lower line).
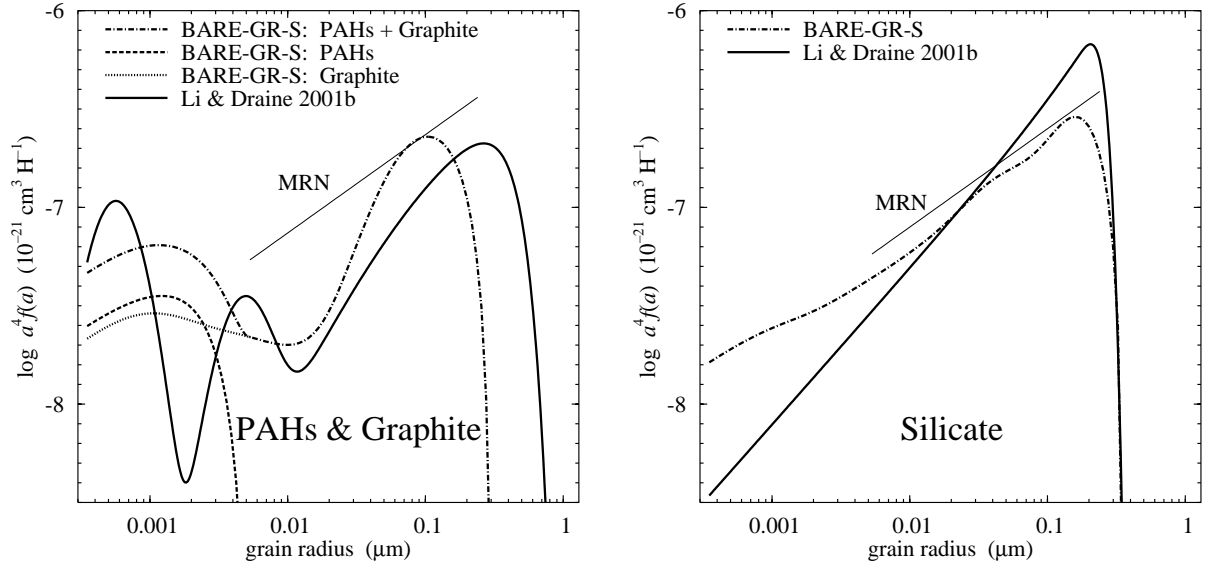
Fig. 18.— COMP-NC-B dust model: the size distributions (top left), extinction curve (top right), elemental requirements (bottom left), and emission spectrum (bottom right). Various populations of the same dust component are depicted by the lines of various width. Two straight lines are the MRN size distributions for silicate (upper line) and graphite (lower line).

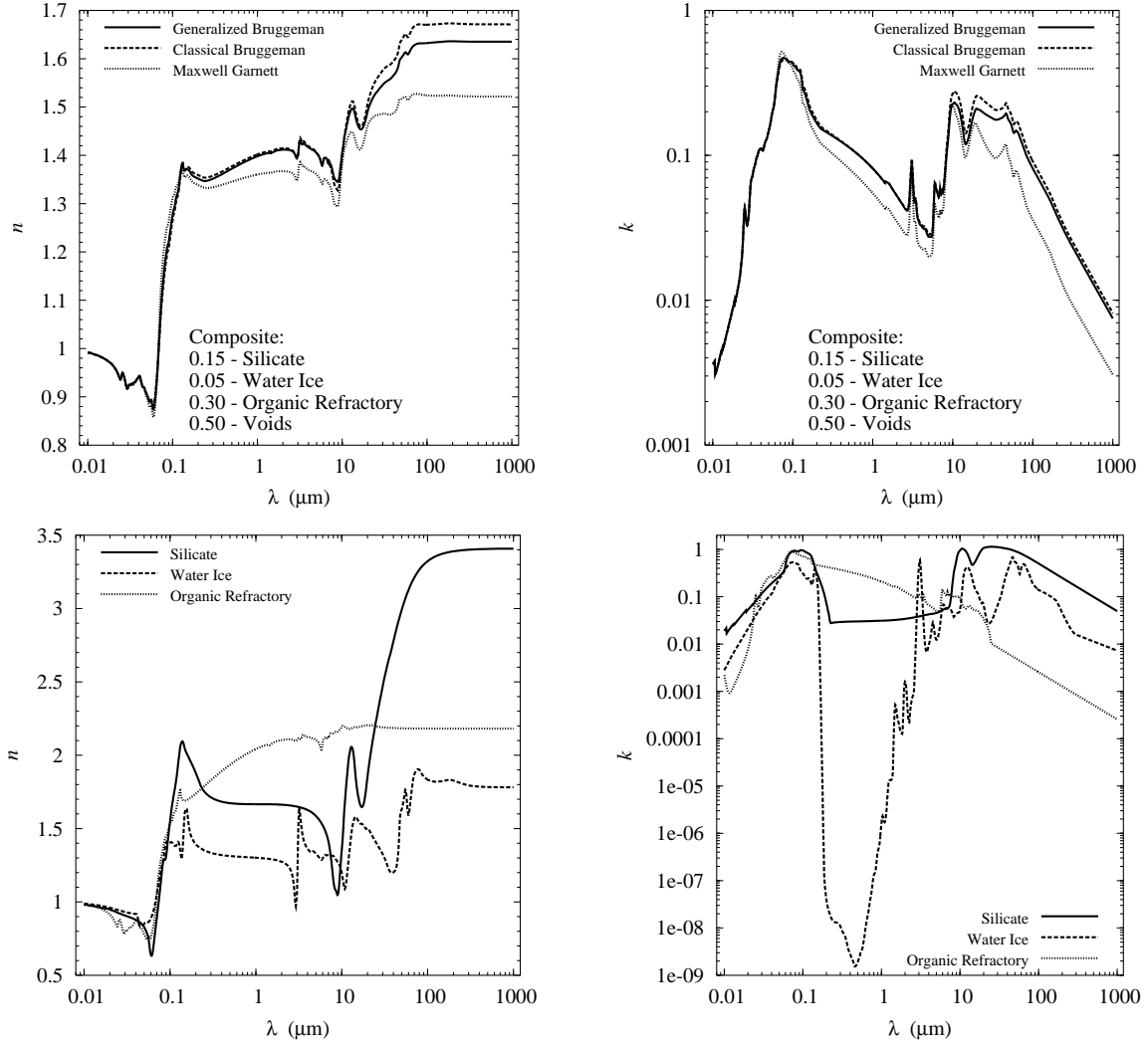Fig. 19.— Grain-size distributions for the BARE-GR-S model compared with the Li & Draine (2001b) size distributions.

Fig. 20.— Optical constants for a composite grain (derived with various mixing rules) and its constituents.
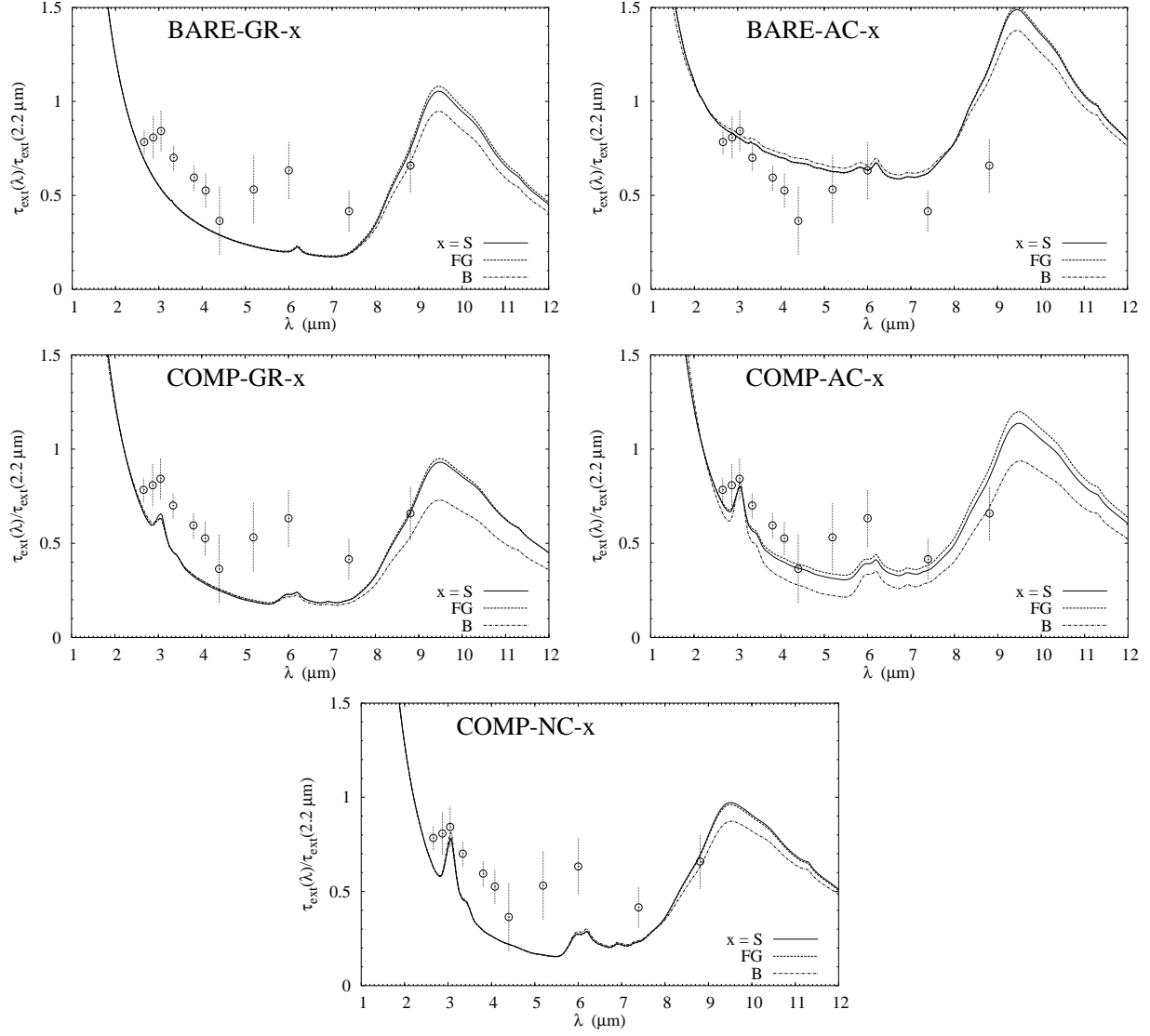
Fig. 21.— Near infrared extinction curves for the dust models. Observational data are for a line of sight toward the Galactic Center (Lutz et al. 1996).
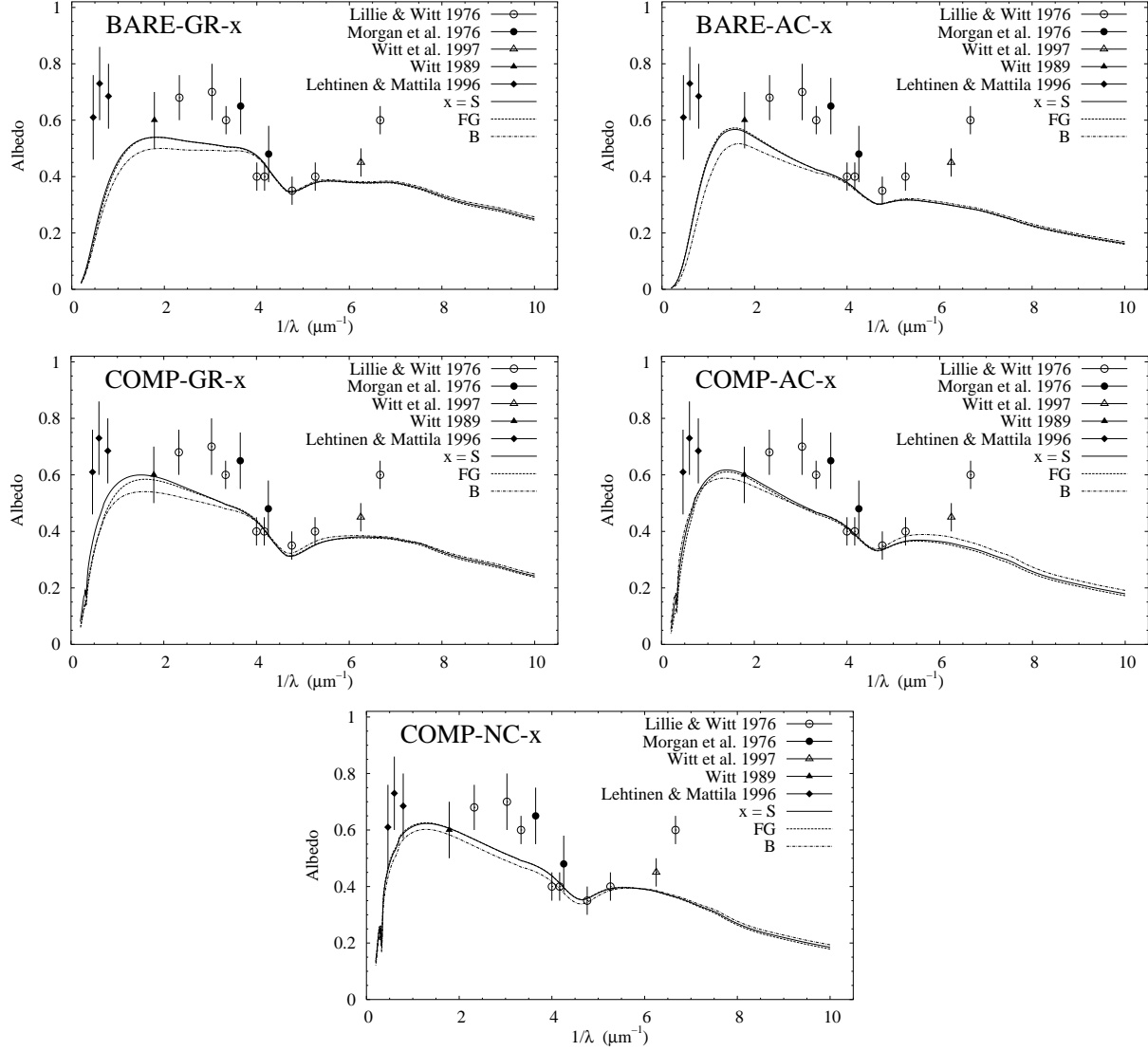
Fig. 22.— Albedo for the dust models along with observational data for the diffuse Galactic light (Lillie & Witt 1976; Morgan et al. 1976; Witt et al. 1997; Witt 1989; Lehtinen & Mattila 1996).
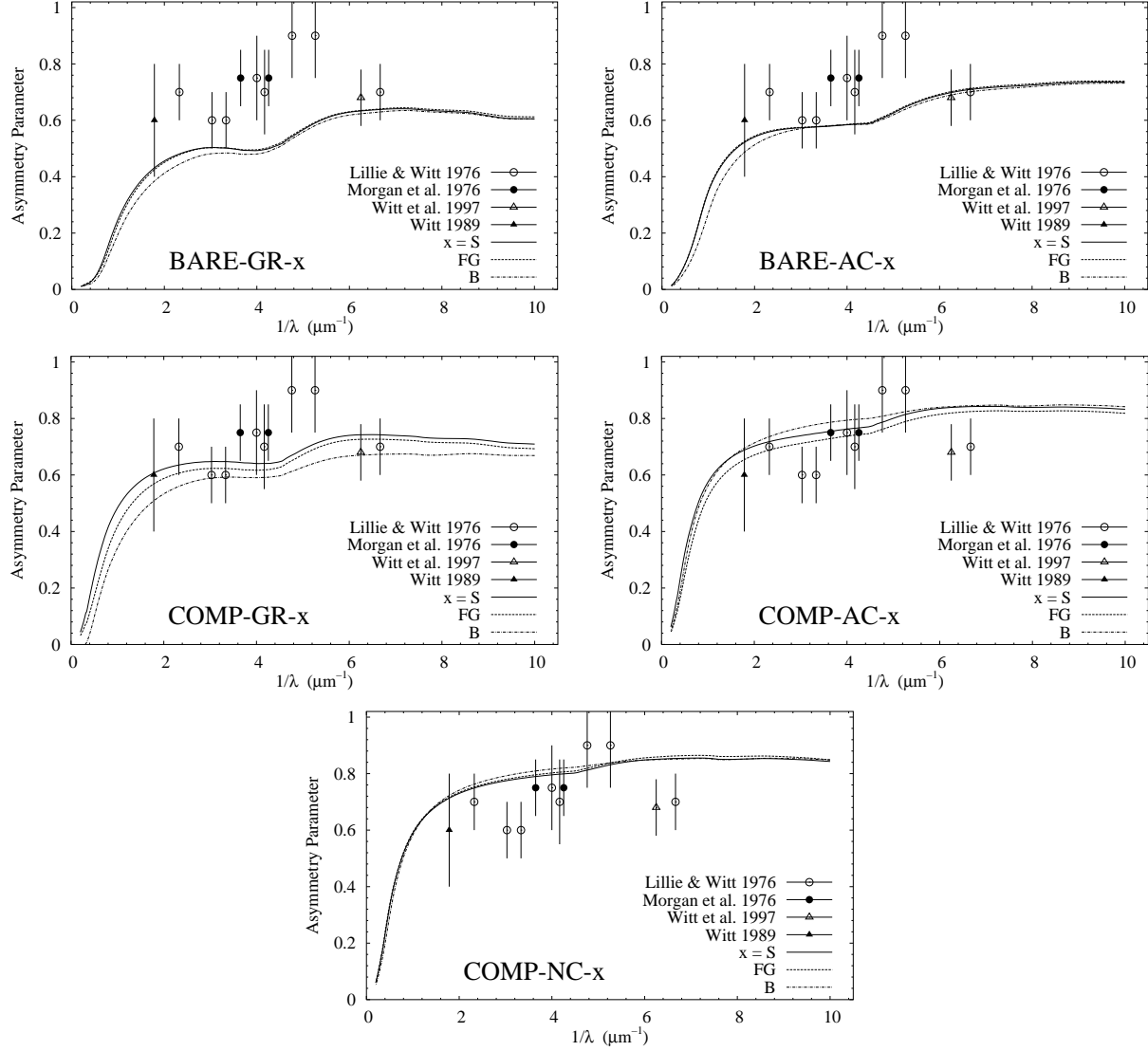
Fig. 23.— Asymmetry parameter for the dust models along with observational data for the diffuse Galactic light (Lillie & Witt 1976; Morgan et al. 1976; Witt et al. 1997; Witt 1989).